Numerical Modeling of Failure in Magnesium Alloys under Axial Compression and Bending for Crashworthiness Applications

by

Usman Ali

A thesis
presented to the University of Waterloo
in fulfillment of the
thesis requirement for the degree of
Master of Applied Science
in
Mechanical Engineering

Waterloo, Ontario, Canada, 2012

I hereby declare that I am the sole author of this thesis. This is a true copy of the thesis, including any required final revisions, as accepted by my examiners.

I understand that my thesis may be made electronically available to the public.

Abstract

Numerical modeling of failure was performed for magnesium alloys with circular and square cross-sections under axial compression. The failure criterion was employed using material model 124, where failure was simulated using the element deletion method. LS-DYNA material model 124 (MAT_124) was calibrated using stress-strain curves in compression and tension. This approach, combined with MAT_124, captures the material asymmetry. Comparisons with experiments showed that the failure criterion accurately predicted the stress-strain behavior during axial compression tests of the round tubes of magnesium alloy, AZ31. A parametric study was also performed to investigate the effects of various phenomena on simulated results. Numerical modeling of square magnesium tubes during bending was also simulated for extruded magnesium alloys AZ31, AM30 and AM60. The failure criterion, based on element erosion, was used in these models to simulate fracture for all three alloys. Comparisons with experiments, for all three alloys, showed that the proposed numerical model accurately predicted the force-displacement curves during bending. Engineering strain at failure was found from the tensile test curves for the three magnesium alloys (AZ31, AM30 and AM60). Simulations were done to predict local strain at the necking region at this engineering strain. The necking strain was incorporated in the failure criterion, which considerably improved results for the bending simulations. Numerical modeling of slow and fast axial compression tests were also performed for AM30, AM60 and AZ31 magnesium tubes with square cross-section. Comparisons with experiments, for all three alloys, showed that the proposed numerical model accurately predicted the force-displacement curves during quasi-static and high-speed crush tests. Furthermore, the predicted fracture locations and patterns were in good agreement with experimental observations. Finally, new failure criteria was employed to improve the crashworthiness behavior of magnesium alloys by several tube design variations. Magnesium tubes cladded with aluminum and magnesium tubes with alternating strips of aluminum were simulated. Magnesium tubes with thinned sections and spirals were also simulated. Results showed that most of the design modifications increased the crashworthiness of magnesium alloys tubes.

Acknowledgements

This work was supported by the Natural Sciences and Engineering Research Council of Canada (NSERC) and General Motors of Canada. I would like to acknowledge Drs. Alan Luo and Raja K. Mishra from General Motors Research and Development, Dr. David Wagner from Ford Motor Company, and the United States Automotive Materials Partnership (USAMP) for providing the experimental data as well as help with using the experimental data. The magnesium experimental data was obtained from the USAMP project Magnesium Front End Research and Development partially funded by the United States Department of Energy. The data from the USAMP project is based on work supported by the Department of Energy: National Energy Technology Laboratory under Award Number No. DE-EE0003583 and a report prepared as an account of work sponsored by an agency of the United States Government. Neither the United States Government nor any agency thereof, nor any of their employees, makes any warranty, express or implied, or assumes any legal liability or responsibility for the accuracy, completeness, or usefulness of any information, apparatus, product, or process disclosed, or represents that its use would not infringe privately owned rights. Reference herein to any specific commercial product, process, or service by trade name, trademark, manufacturer, or otherwise does not necessarily constitute or imply its endorsement, recommendation, or favoring by the United States Government or any agency thereof. The views and opinions of authors expressed herein do not necessarily state or reflect those of the United States Government or any agency thereof. Such support does not constitute an endorsement by the Department of Energy of the work or the views expressed herein.

I would also like to thank Dr. Raja K. Mishra for his technical expertise and for providing the experimental data for round tubes with circular cross-sections. I would also like to thank Jonathan Rossiter for help with the failure criteria. Finally, I would like to thank my supervisor Prof. Kaan Inal for his supervision and guidance.

To family and friends.

Table of Contents

List of Figures

List of Tables

Chapter 1
Introduction

The economic and environmental benefits of increased fuel economy and reduced emissions are constantly driving auto sector to reduce the vehicle weight. In this regard, light metals such as Aluminum (Al) and Magnesium (Mg) alloys, are attractive candidates for automotive parts [2,3,4]. Magnesium has similar mechanical and physical properties as aluminum alloys but it is nearly one third lighter. Magnesium sheet alloys offer less ductility than common aluminum alloys but offer similar strength [5]. However, magnesium alloys are expensive and have much less formability [5]. New magnesium alloys have better formability and are being tested for implementation in automotive applications [6].

Currently, there are some automotive manufacturers who use magnesium alloys for body parts [7]. Even though magnesium components are being used more and more, the amount of magnesium use compared to aluminum and polymers is still very low [8].

Safety or crashworthiness of the car body is a very important aspect of automobile design and therefore needs consideration before the final product is developed. Today, the automotive industry uses advanced numerical analyses and design software to simulate different loading conditions to verify their designs before they are ever put in the final product. Therefore, the ability to predict magnesium failure is crucial for engineers to use magnesium alloys in different parts of the vehicle related to crashworthiness. While experiments for crashworthiness are very expensive and time consuming, the three tests below can be used to investigate the material behavior under bending and crush.

a) Four point bending test

b) Slow axial crash

c) Fast axial crash

These results are used to evaluate the crashworthiness of a material. The response of a material is presented as a force-displacement curve and the area under this curve represents the energy absorbed by a material under crash before failure. Unlike aluminum and steel, magnesium is a brittle material

and tends to fracture under axial loading and bending [9]. Therefore a material model capable of predicting failure is necessary to simulate magnesium alloys under different loading conditions.

There are a number of Finite Element Methods (FEM) to predict failure employing different frameworks. Three of the most commonly used ones are the extended finite element method (XFEM), the interelement crack method and the element deletion method [10]. In this research, element deletion method coupled with a set of deletion rules for each element was employed to simulate fracture in various magnesium alloys. It is noted that magnesium alloys present unique challenges due to their tension-compression asymmetry. Thus, they exhibit different failure characteristics under compression and tension.

There are various approaches to predict failure that are useful in metal forming and crashworthiness simulations. Examples of failure criterion used to simulate fracture include constant equivalent strain, maximum shear stress, forming limit diagrams (FLD) and the Johnson Cook model. In this paper, a new failure criterion is employed to predict magnesium failure [1].

This paper presents a study of failure in three different magnesium alloy tubes; AZ31, AM30 and AM60. The tubes are submitted to four point bending, slow and fast axial crush tests. The dimensions of the tube are given in Section 5.1. AZ31 and AM60 tubes have rivets in the flange while AM30 does not have these rivets. The tubes are very close to squares with a side length of 160 mm, 2.5 mm thickness and 400 mm long. Exact dimensions of the cross section are presented in Section 5.1. Round tubes with circular cross sections are also employed for crush tests. The criteria presented by Rossiter et al. [1] were modified for the simulations in this research. The failure criteria uses the existing strain failure criteria in MAT_124 and additional failure criterion (developed for this research) that were incorporated into LS-DYNA. A new failure criteria involving necking strain was also implemented in the model to improve results. The deformed specimens obtained from experiments and numerical simulations [9,11,12] were compared for axial crush and four point bend tests.

Experiments for AZ31 were performed for only round tubes with circular cross-sections and stress-strain values were recorded for these experiments. Experiments were also performed for AM30, AM60 and AZ31 for four point bend tests and axial crush. Axial crush tests involved slow and fast

crush tests for all three alloys. Bend tests had two rollers on the top and two rollers at the bottom of the tube. There were end plates in the tubes for all the experiments. Crush experiments consisted of fixed and moving ends. The square tubes had end plugs to keep the tubes in place during the experiment where load-cross-head displacement data was recorded for all experiments.

Simulations with the new failure criterion were performed for axial crush tests. A parametric study was performed on the round tubes to investigate the effects of imperfections, boundary conditions, load curves, time scaling, hourglass and damping on failure. The purpose for the study was to find the simulation conditions that would give the best results compared to the experimental results since the experimental conditions were not always clearly defined. A combination of all the parameters was found to give the best results. Axial crush and bending simulations for the square tubes were also performed with the failure criterion where solid brick elements were used with multiple elements in the through thickness to simulate failure. The predictions from the round tube (with and without the parametric study) were compared to the experimental results. The final simulation results predicted the initial force jump, the trend and the maximum force with reasonable accuracy.

The slow and fast axial crush test simulations were compared to experimental observations for force-displacement curves and deformed specimens. AZ31, AM30 and AM60 slow and fast axial crush simulations predicted the failure points, the bulge near the crush triggers and the deformation pattern accurately. Simulations also predicted the trends and peak forces in the force-displacement curves for most cases.

The four point bend tests were also compared to experiments using the force-displacement curves and deformed specimens. The four point bend tests were also carried out for all three alloys. AZ31, AM30 and AM60 simulations showed dimples and failure in the tubes. Comparisons of predictions from simulations and experiments for force-displacement curves showed that the simulations predicted the peak force and trends accurately. Furthermore, the new criterion (from fracture strain simulations) correctly predicted the behavior for AM30. The simulation results with and without fracture strain clearly show improvement in the prediction of peak force and the overall trend.

Finally, the new failure criterion was used to “perform virtual testing” for new designs of round tubes of magnesium alloys AM30, AM60 and AZ31. Magnesium tubes with thinned sections and spirals (along the length of the tubes) were simulated along with magnesium-aluminum cladded and magnesium-aluminum alternating (in length) tubes. The simulations were compared to each other and the initial round tube using stress-strain curves from different design modifications for

crashworthiness applications. Results show improvement in crashworthiness applications for AZ31 and AM30 for most designs while AM60 did not show a considerable improvement for any of the suggested designs.

Chapter 2
Background

This chapter discusses the magnesium material properties. The chapter also talks about the magnesium alloys that are presented in this paper. Applications of magnesium alloys with examples are also presented. Finally, different failure criteria that are currently being used in industry and different finite element methods to simulate problems of fracture and failure are presented.

2.1 Material Properties

Magnesium has a hexagonal closed-packed (HCP) crystal structure. Iron and aluminum, on the other hand, have a face-centered cubic (FCC) crystal lattice structure. Figure 1 shows the principle planes and directions in the magnesium unit cell. Magnesium alloys present a tension-compression asymmetry. This asymmetry in wrought magnesium parts is due to deformation twinning [13]. At high temperatures new slip systems become active in magnesium alloys which provide improved formability.

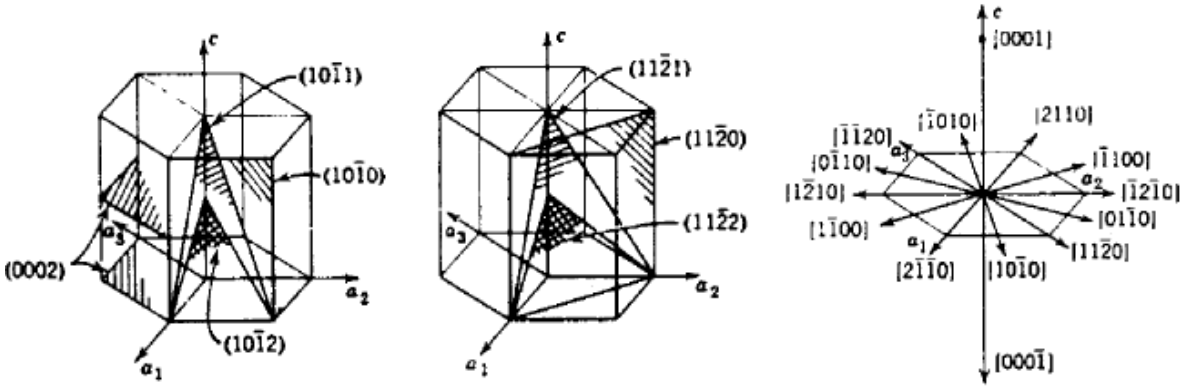

Figure 1: Principle planes and directions in the magnesium unit cell [14]

Magnesium's atomic diameter is approximately 0.320 nm. This allows it to form a solution with many metals like Al, Zn, Ag, Zr, etc. The ability to form a solution with many metals makes different types of alloys possible. General chemical compositions of AM30, AM60 and AZ31 are given in Table 1-3. Other metals like iron, copper, nickel and silicon are also present in these alloys in minute weight quantities. Mg-Al alloys allow for ease of extrusion while Mg-Li alloys present higher ductility [15].

Table 1: Chemical Composition of AZ31 (wt %) [16]

Al	Zn	Mn	Mg
3.1	0.92	0.41	Bulk

Table 2: Chemical Composition of AM30 (wt %) [17]

Al	Zn	Mn	Mg
3.4	0.16	0.33	Bulk

Table 3: Chemical Composition of AM60 (wt %) [18]

Al	Zn	Mn	Si	Mg
5.8	0.01	0.30	0.01	Bulk

Wrought magnesium alloys show anisotropic behavior at room temperature. This anisotropy is mainly due to forming processes like rolling, drawing and extrusion [19]. Magnesium alloys retain the deformed texture from these forming operations and this contributes to anisotropy [20]. Other causes of anisotropy are: residual stresses, laminar inclusions and cavities [19]. A method to reduce this anisotropy in magnesium alloys is to anneal the material. Annealing helps reduce the texture and increase the grain size [21]. While some research focuses on the minimization of the anisotropy of magnesium alloys, other research focuses on modeling the anisotropic material behavior. Cazacu 2006 yield surface, for example, suggests a yield surface that predicts the anisotropic behavior of magnesium alloys [22]. However, determining the material parameters and fitting experimental data to yield surfaces are time-intensive.

Magnesium alloys were in use since the Second World War [15] with primary focus on sheet products. Over the next two decades, the use of magnesium increased drastically. Currently, automotive companies show great interest in using magnesium for automotive applications. Magnesium is lighter than conventional metals, which makes it a prospective automotive component. Figure 2 and Figure 3 show the mass savings potential of various materials with respect to mild steel

for designing a structural beam and panel. Figure 2 and Figure 3 present data for advanced high strength steel (AHSS), aluminum (Al), magnesium (Mg), plastic blend of polycarbonate (PC/ABS), glass fiber reinforced polymers (GFRP) and carbon fiber reinforced polymers (CFRP). Figure 2 and Figure 3 only analyze the mass savings potential for bending conditions as bending is the primary strain path in most automotive applications. In almost all cases, magnesium presents more than 50% mass savings. This is the main weight advantage of using magnesium over most metals.

Magnesium alloys present properties that are totally different than the usual automotive materials. Magnesium provides more elongation compared to polymers, allowing engineers to use magnesium in scenarios that require high ductility and crashworthiness [7]. However, magnesium alloys exhibit different stress-strain characteristics under tension and compression at room temperature. Magnesium also offers better performance than aluminum alloys at high temperatures with higher thermal expansion and lower thermal conductivity.

The general corrosion resistance of magnesium is also better than the aluminum alloy 380 [7] however magnesium has high galvanic corrosion problems. The problem is solved by using magnesium with other non-conductive metals. This method has been in practice for some time now where General Motors (GM) and Ford use the same method for the transfer case of Four Wheel Drive (4WD) system [7]. Another way to save magnesium from galvanic corrosion is to use chemical coatings like Alodine 5200 [7].

Magnesium alloys are hot extruded to make different parts [23]. Magnesium alloy AZ31 is used in various automotive applications and is discussed later in this research. Magnesium alloys AZ61 and AZ80 have higher aluminum contents but are less likely to be used for extrusion due to lower extrudability than AZ31. There are also high-strength magnesium alloys like ZK60, which are used in race cars and bicycle wheels [24]. Extruded AM30 has higher ductility than AZ31 at room temperature and is also discussed in this research.

Hydroforming is used to make various perimeter shapes out of magnesium tubes. Hydroformed parts have a number of applications like engine cradle, frame rail and radiator support [7]. Hydroforming of magnesium tubes at room temperatures is very limited and generally requires high temperatures (150-200^{o}C) [25].

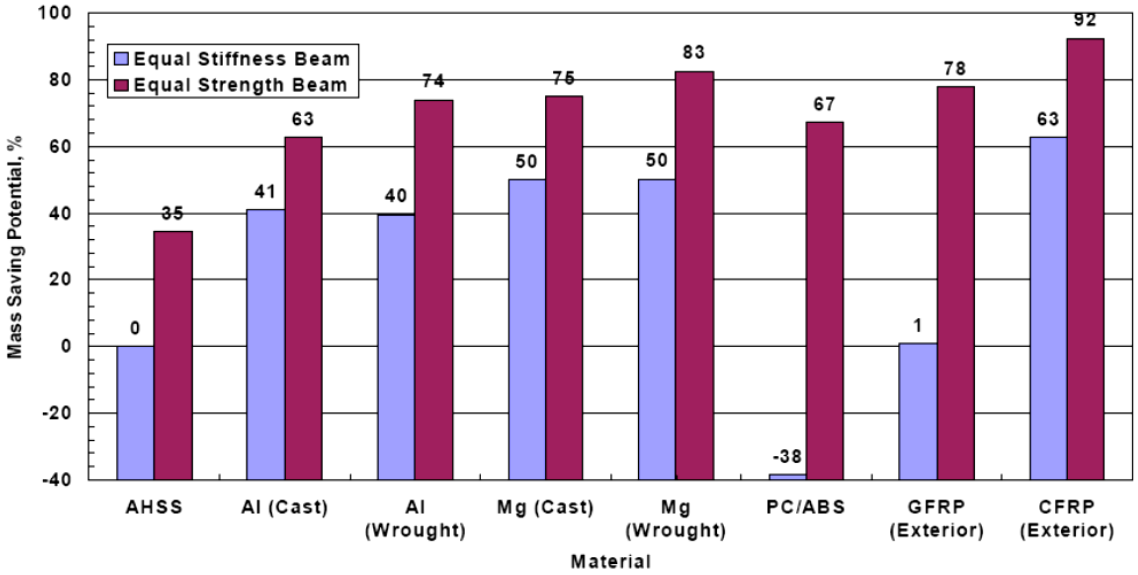

Figure 2: Percentage mass savings of various materials vs. Mild steel for designing a structural beam with equivalent bending stiffness or bending strength [7]

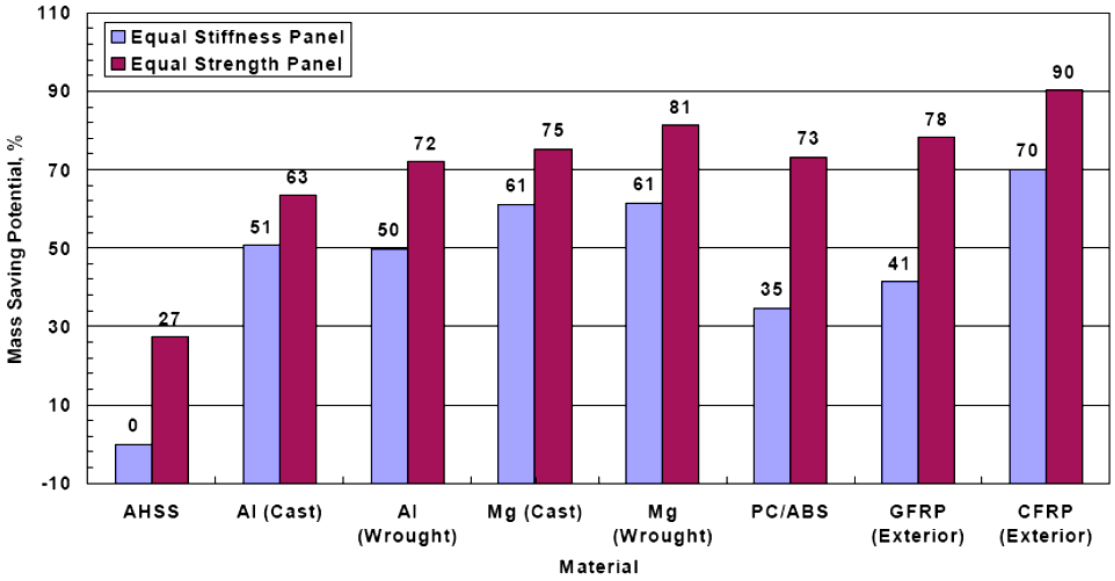

Figure 3: Percentage mass savings of various materials vs. mild steel for designing a structural panel with equivalent bending stiffness or bending strength [7]

Magnesium sheets are also warm formed to make parts for different industries. The average temperature is approximately 350^{o}C. Forming at lower temperatures was also achieved by GM [25]. Other forms of magnesium forming include superplastic forming which are used to make door inners [26].

Cast magnesium parts have a lot of industrial applications. Magnesium alloys show high fluidity, which allows for thinner cast walls [5] that do not stick to the iron die parts, which results in a cleaner part. Magnesium alloys also have a low specific heat, which results in faster cycle times and low die wear.

2.2 Failure Criteria

A significant amount of research was done in different failure criteria used in industry to simulate failure of materials [27]. Some examples of failure criteria are: Constant equivalent strain [28], Maximum shear stress criteria [28], Freudenthal model [29], Cockcroft-Latham failure criteria [29], Brozzo model [30], Ghosh model [31], Norris model [32], Oyane model [33], Atkins model [34], Wilkins model [35], Johnson-Cook model [36], Xue-Wierzbicki model [28] and Forming Limit Diagrams [37]. Some of these models that are relevant to this research are explained below.

2.2.1 Constant Equivalent Strain

This failure model assumes fracture when the equivalent plastic strain, $\bar{\epsilon}$, reaches a critical value, ϵ_c. For an incompressible material, the equivalent plastic strain is defined in terms of the principal strains [38]. The failure criterion employed in this thesis uses this failure criterion as one of the criteria for failure predictions.

2.2.2 Maximum Shear Stress Criterion

This failure model is based on bulk material properties [39,40]. It assumes that a ductile fracture (Figure 4) will occur when the shear stress on a plane is maximum. Failure is assumed when τ_{max} is equal to or greater than $\tau_{max,f}$. τ_{max} is calculated using the average of the three principal stresses and finding the maximum value. This is similar to the Tresca yield condition.

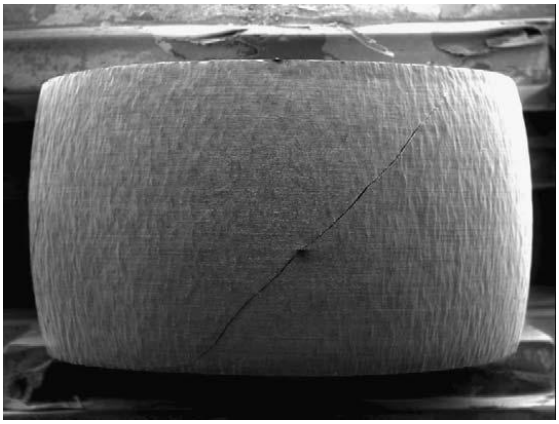

Figure 4: Shear fracture in a specimen of 2024-T351 A1 [27]

2.2.3 Johnson Cook Fracture Model

In the Johnson Cook model, fracture is assumed to take place when the equivalent fracture strain exceeds the critical value [36]. The criterion assumes that equivalent fracture strain is a monotonic function of the stress triaxiality (η). Stress triaxiality parameter is a ratio of average stress to the equivalent stress.

2.2.4 Xue–Wierzbicki Fracture Model

The Xue Wierzbicki model assumes fracture when the plastic strain, modified by the function of stress triaxiality and the deviatoric state parameter reaches a limiting value of 1 [28]. The model defines limits on the upper and lower bounds of the axisymmetric stress state which is used to find the function that modifies the plastic strain. The final modification function ends up being a function of four parameters C_1, C_2, C_3 and C_4. These parameters are found using experimental data. C_1 and C_3 are found using the axisymmetric and plane strain conditions while C_2 and C_4 are the hardening exponents in the final equation [27].

2.2.5 Forming Limit Diagram (FLD) Fracture Model

Formability in sheet metal forming is limited by the onset of localized necking in the material [37]. An important tool to find the onset of necking is FLD's. A FLD is a plot of major and minor principal strains. These strains are computed where localized instability in a plane stress condition occures. This data is plotted based on different ratios of major and minor strains [41]. Experimental determination of FLD's requires extensive experimentation and is therefore time consuming. However, interest in this field resulted in many theoretical methods. Marciniak-Kuzynski (M-K)

Analysis is one of the methods used to theoretically predict the onset of necking. [42]. Figure 5 shows a FLD for eleven different materials where the curves are normalized with the plain strain fracture strains [27].

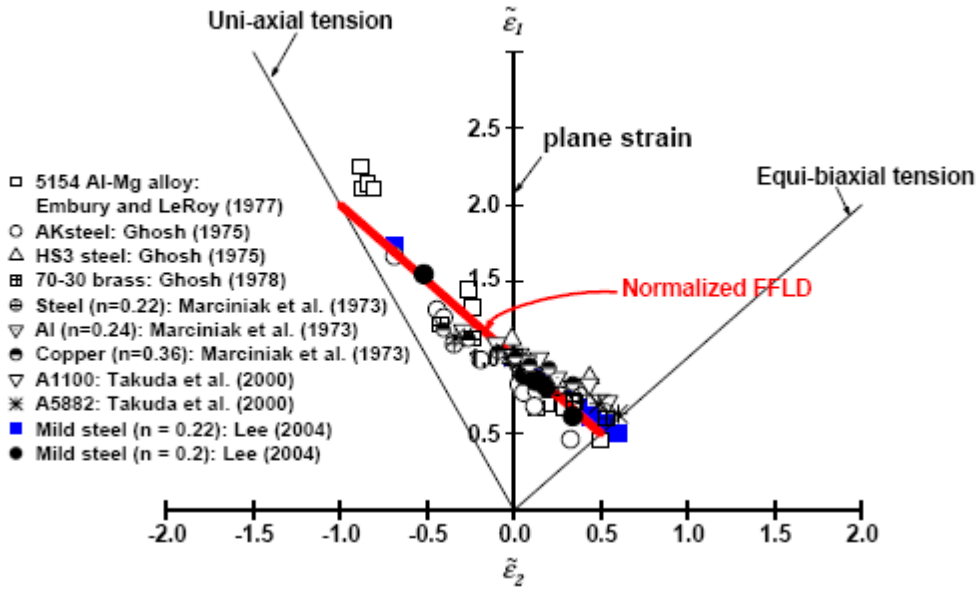

Figure 5: Normalized FLDs for 11 different materials in punch indentation problems [27]

2.3 FE Methods

There are three main approaches: Element Deletion, Extended Finite Element Method (XFEM) and Interelement Crack Method, that are employed in finite element analyses to investigate problems involving fracture and failure. However, new approaches such as meshless methods (EFG) are emerging as powerful tools that can be used to investigate failure in structures. All the methods above solve a finite element ordinary differential equation with minor changes to its implementation in the code. These four methods are briefly summarized below.

2.3.1 Element Deletion Method

This research employed the element deletion method to simulate the material response under axial crush and bending since it was the most efficient method (in terms of CPU time) compared to the others. This thesis presents a study on macro-scale failure modeling and thus, CPU time is an important parameter. Contrary to the element deletion method, XFEM and EFG simulations usually require at least twice as much CPU time for macro-scale failure modeling.

Element deletion method works on a normal finite element code. Element deletion methods were mainly created to predict fracture in materials [10,43]. As the size of element increases or decreases, the ability to predict crack growth decreases and increases respectively. In addition, element deletion methods fail to predict multi-crack growth in some cases. For this reason, element deletion is not used for crack propagation applications.

Commercial software, LS-DYNA, refers to a failure criterion at the end of each step which decides to delete or keep an element. LS-DYNA removes the element but keeps the mass constant to avoid the inertial effects caused by removing elements [10].

Element deletion methods are used in the field of machining [44,45] to simulate crack initiation, shearing and multi-pass hot bar rolling [45]. Element deletion methods can simulate chip formation for orthogonal machining problems under these processes. Figure 6 shows the initial stages of how the chip forms when the tool hits the surface.

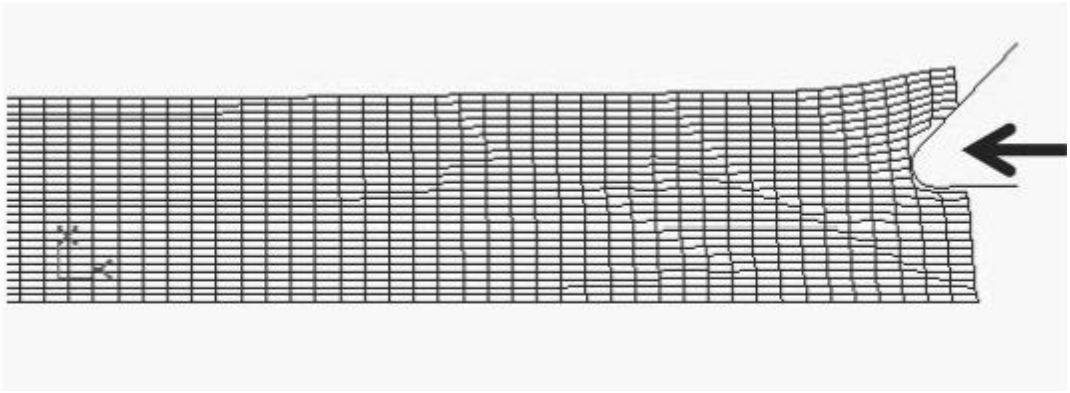

Figure 6: Element Deletion to Simulate Chip Formation [45]

Furthermore, element deletion methods are often used in metal forming applications. However, magnesium is unlike many other commercial metals since it does not behave similarly under tension and compression. Thus accurate predictions of failure in magnesium alloys can't be obtained with current failure criteria that exist in literature. Hence, a new criterion based on the work presented by Rossiter et al. [1] was employed to predict magnesium failure.

2.3.2 Extended Finite Element Methods (XFEM)

Extended Finite Element Methods (XFEM) were also developed to predict crack propagation and induction in materials [46,47]. The key idea in this finite element method is that the displacement equation incorporates the crack discontinuity as additional terms in the formulation. The displacement in an XFEM problem is given in Equation 1 [10].

$$u^h(X,t) = \sum N_I(X)\{u_I(t) + H\big(f(X)\big)H\big(g(X,t)\big)q_I\} \qquad (1)$$

Where $N_I(x)$ is a shape function, and u_I and q_I are the regular and enriched nodal values respectively. Functions f(x) and g(x) define the crack geometry as shown in Figure 7.

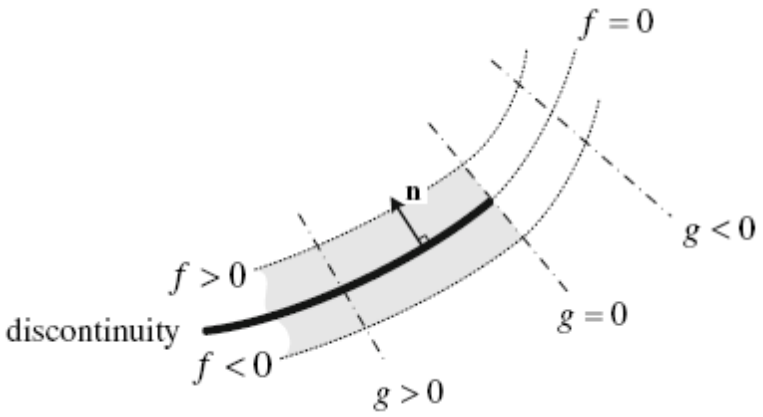

Figure 7: Discontinuity Representation in XFEM [10]

H(f(x)) is the Heaviside function which is active only when f(x) is greater than zero. Note that u_I is not the displacement at the node. However, XFEM-based codes shift the approximation on q_I so that u_I represents the nodal displacement of each element.

The disadvantage of this method is the time constraint and the inability to predict crack speeds unless the model is tuned with the experimental results. Another problem with XFEM is that the user has to input the discontinuity on the basis of some failure criterion. In addition, XFEM tends to favor a single crack profile rather than multiple cracks [10].

2.3.3 Interelement Crack Method

The interelement crack method is another approach used to simulate cracks with different formulations [48,49,50]. The basic formulation assumes that all nodes are not connected from the beginning, as shown in Figure 8. The nodes on the edges are mechanically held together by cohesive forces. These forces are governed by cohesive laws based on tangential and normal traction components.

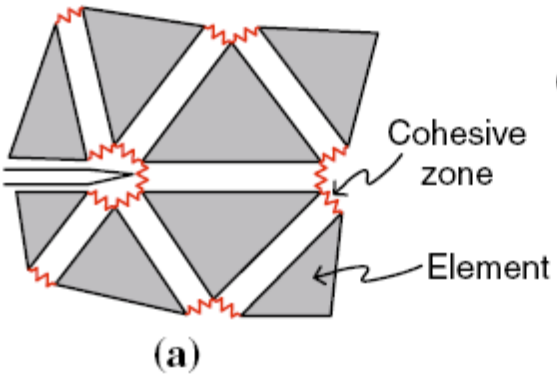

Figure 8: Interelement Crack Method [10]

This method is mainly used for crack propagation problems. The disadvantages are increased computational time and inability to predict crack propagation speeds for edge-crack and dynamic crack propagation problems.

2.3.4 Element Free Galerkin Method (EFG)

EFG method is a new and emerging finite element method [51]. A standard finite element method uses a mesh with elements and nodes. EFG methods, however, only use nodes to simulate problems. This makes meshing an EFG problem very easy. Another advantage of EFG is that it eliminates the problem of re-meshing in high deformation problems since it does not have any elements. The concept of EFG is based on the partition of unity method [52]. The elements in EFG are called cells which are calculated based on the problem definition rather than user definition of each element. These cells can also change during the simulations. A sample of circular cells in a given domain is shown in Figure 9.

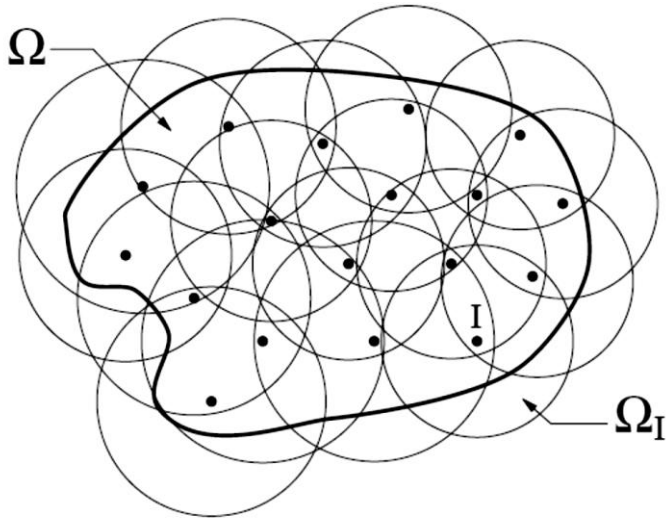

Figure 9: EFG Cells in a sample [53]

EFG weight functions are generally more complicated than finite element weight functions and are available as exponential, cubic and quartic-spline functions. To approximate the solution, EFG methods normally use moving least squares method that provides ease in approximating the accuracy of the solution based on the monomials used (Equation 2) [53].

$$u^h(x) = \sum_{i=1}^{m} p_i(x) a_i(x) = p^T(x) a(x) \qquad (2)$$

Where p_i are the components of the monomial basis function and a_i are their coefficients. The EFG problem simplifies to a set of integrals like any other finite element problem. The main difference in solving EFG problems when compared to finite element problems is that EFG codes usually loop on each quadrature point while finite element simulations loop on each element. The main disadvantage of the EFG method is its unavailability in current commercial software. LS-DYNA however, has some sort of EFG implemented in its code. EFG also requires very large CPU time; simulations with EFG can take 2-3 times more CPU time compared to a "classical" FE code for the same problem.

Chapter 3
Material Properties and Material Model

This chapter discusses the material properties of AM30, AM60 and AZ31 magnesium alloys. Stress-strain curves in compression and tension are given for all three alloys. MAT_124 is also discussed in this chapter along with the failure criterion used in this paper.

3.1 Material Properties

Magnesium alloys show different stress-strain responses under tension and compression at room temperature as shown in Figure 10, Figure 11 and Figure 12. Experimental stress-strain responses for all three alloys are different under compression and tension. This tension-compression asymmetry in the material makes it harder to simulate the material response using material models that cannot account for this phenomenon. Composition of magnesium alloys is given in Section 2.1.

AZ31 experimental compressive and tensile stress-strain curves (Figure 10) show that initially, there is more tensile stress than compressive stress for the same strain until 230 MPa stress at 7% strain. After that, the compressive stress is greater than the tensile stress for a given strain. Both the tensile and compressive curves then saturate at around 250 MPa and 350 MPa, respectively, for approximately 28% and 26% strain respectively.

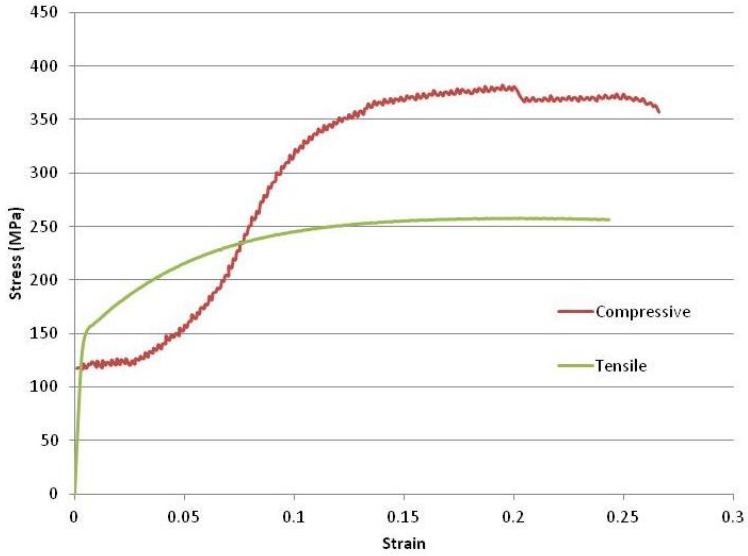

Figure 10: Magnesium AZ31 Stress-Strain Curves under Compression and Tension

AM60 experimental compressive and tensile stress-strain curves (Figure 11) show that initially, the stress strain responses under compression and tension are the same up to 0.5% strain and 130 MPa stress. After this point, there is more compressive stress than tensile stress for the same strain levels. For the compressive stress-strain curve, the material fails at approximately 8% strain and 320 MPa stress. For the tensile stress strain curve, the material fails at approximately 12% strain and 280 MPa stress.

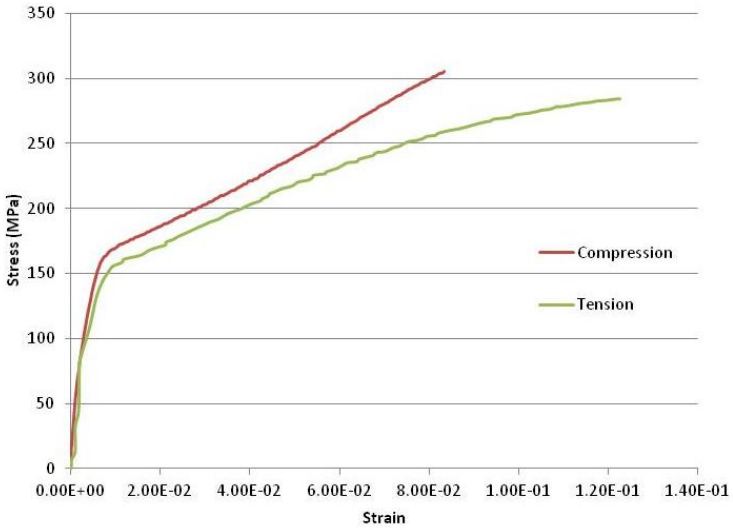

Figure 11: Magnesium AM60 Stress-Strain Curves under Compression and Tension

AM30 experimental compressive and tensile stress-strain curves (Figure 12) show that the tensile stress is higher than the compressive stress for a given strain until 12% strain and 220 MPa stress. After this point, the material looses a little tensile strength as strain increases to around 13%. The compressive stress increases until the final value of roughly 21% strain and 240 MPa stress.

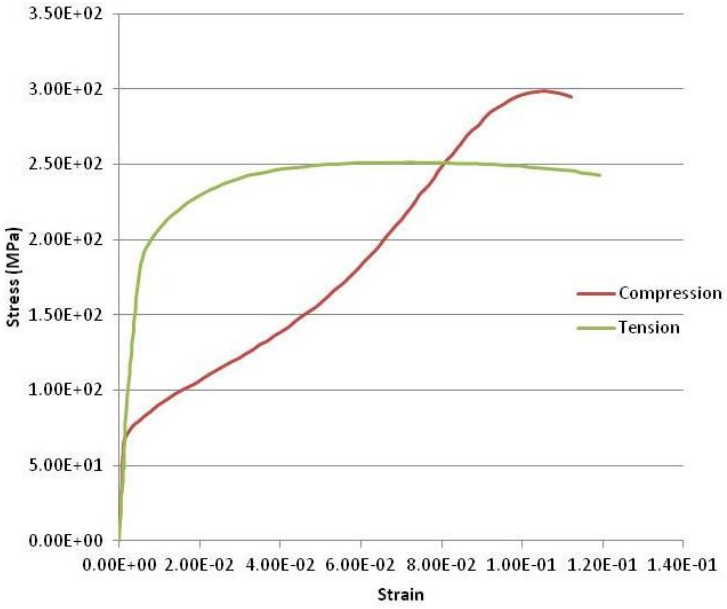

Figure 12: Magnesium AM30 Stress-Strain Curves under Compression and Tension

Using the material model (MAT_124) in the commercial software LS-DYNA, separate tension and compression curves were inputted for each of the above-described magnesium alloys [54]. Separate tension and compression curves account for the asymmetry of the material under different loading conditions in this material model. It is noted that the material model (MAT_124) allows the user to specify different stress-strain curves as well as a user-defined subroutine to specify the failure criteria for the elements. LS-DYNA checks this subroutine at the end of every time step to fail or to keep an element. This subroutine was modified to predict the material behavior under axial loading and bending. The material properties used for all the numerical simulations are given in Table 4.

Table 4: Material Properties

Property	Density	Young's Modulus	Poisons Ratio
Value	1.77 g/cm^3	45 GPa	0.30

3.2 Material Model

Commercial software LS-DYNA provides users the option to use different material models. Material model 124 was used for all the simulations presented in this research. Figure 10, Figure 11 and Figure 12 show that the compression and tension responses for all three magnesium alloys are different. MAT_124 allows the user to input two separate stress-strain curves to account for the asymmetry in the material.

MAT_124 (Tension-Compression Plasticity) is based on MAT_10 (Elastic-Plastic Hydrodynamic) and employs a Von Mises-type yield function. Von Mises yield function assumes isotropic material properties. MAT_124 assumes isotropic asymmetric material in its formulation and uses the Jaumann rate of the deviatoric stress (Equation 4) and the hypo-elasticity model (Equation 3) to derive the constitutive equations [54,55,56]. In Equations 3 and 4, $\dot{s}_{ij}$is the deviatoric stress rate, $\dot{s}_{ij}^{\mathrm{j}}$ is the Jaumann rate of deviatoric stress, G is the shear modulus and $\Omega_{pj}$is the spin tensor.

$$\dot{s}_{ij}^{\mathrm{j}} = 2\mu\dot{\varepsilon}_{ij}^{j} = 2G\dot{\varepsilon}_{ij}^{j} \quad (3)$$

$$\dot{s}_{ij}^{\mathrm{j}} = \dot{s}_{ij} - s_{ip}\Omega_{pj} - s_{jp}\Omega_{pi} \quad (4)$$

MAT_124 uses radial return (Equation 6) to scale the effective trial stress back on the Von Mises yield surface using Equation 5. In Equations 5 and 6, σ_y is the yield stress and $\tilde{s}$ is the effective trial stress.

$$\frac{1}{2}\, s_{ij}\, s_{ij} - \frac{\sigma_y^2}{3} \leq 0 \quad (5)$$

$$s_{ij}^{n+1} = \frac{\sigma_y}{\tilde{s}}\, \tilde{s}_{ij}^{n+1} \quad (6)$$

Plastic strain is found by subtracting the elastic or the deviatoric part of the strain increment from the total deviatoric increment. Hardening is calculated based on the input tensile and compressive curves. MAT_124 calculates the mean stress (pressure) to decide if the material is under tension or compression. The increment in plastic strain is calculated using Equation 7 where $\Delta\epsilon^p$ is the increment in plastic strain.

$$\Delta\epsilon^p = \frac{\tilde{s} - \sigma_y^n}{3G + E^p} \quad (7)$$

MAT_124 is summarized in a few steps as follows. Under plastic loading, MAT_124 calculates the plastic strain increment and then updates the total plastic strain and yield stress based on the input curves. MAT_124 then returns the yield stress back to the yield surface using radial return and computes the new stress.

MAT_124 is used to account for strain rate dependence by employing the Cowper and Symonds model. This model is used to scale the yield stress based on a factor provided in the LS-DYNA Theory Manual [56] and is shown in Equation 1.

$$1 + \left(\frac{\dot{\varepsilon}}{C}\right)^{\frac{1}{p}} \quad (1)$$

where $\dot{\varepsilon}$ is the strain rate calculated by Equation 2 [56] and *C* and *p* are strain rate parameters.

$$\dot{\varepsilon} = \sqrt{\dot{\varepsilon}_{ij}\dot{\varepsilon}_{ij}} \quad (2)$$

Tensile and compressive experiments were done at different strain rates (bending, slow and fast axial crush) for all three magnesium alloys. Stress-strain curves obtained from tensile and compressive experiments were used as inputs to MAT_124. The average strain rate of the tensile-compressive experiments and simulations were the same and hence, C and p were taken as 0.

3.3 Failure Criteria

The failure criterion employed in this research is based on the work presented by Rossiter et al. [1]. There are three simultaneous failure criteria implemented in all the models. The first criterion removes an element if the strain within an element reaches a higher value than the lowest failure strain observed in the experimental tension/compression stress-strain curves. The criterion only deletes an element if the hydrostatic stress is greater or less than zero depending on whether the lowest failure strain is tensile or compressive respectively. The second criterion removes an element if the stresses acting on the two parallel faces of a quadrilateral element are more than the sum of the ultimate tensile stresses from the tensile and compressive stress-strain curves. The last criterion removes an element if the strain exceeds the fracture strain of the material.

Another explanation for the criteria given in [1] is that the failure criterion was a result of the delay in buckling seen in the magnesium tubes. Prior to the tube buckling, the strain is sufficient enough to cause twinning, represented by the crossover point in AZ31 (Figure 10) and AM30 (Figure 12). When buckling begins, the outer edge of the material changes from compressive to tensile stress. This change from compressive to tensile stress is experienced by the outer elements of the tubes. The difference of the resulting stress on the opposite side of each element, when compared to fully integrated elements, shows that damage would have occurred in the material. The damage occurs when the difference in the stresses is greater than the ultimate tensile and compressive strength of the material.

The failure criterion can also be explained using hardening curves [57]. An element is eroded based on its hardening history under tension and compression. Since buckling is the main cause of failure, the hardening history was taken from two opposite sides of an element with the element axis parallel to the buckling direction. The area under the hardening curve (hardening rate vs. strain) was computed and compared to a critical value. This critical value was calculated from uniaxial compression and tensile tests and equates to the sum of the area under the hardening curves under tension and compression.

3.4 Failure Strain

The macroscopic failure strain is typically used to predict failure in FEA simulations. However, finite element softwares usually calculate true strain at every time step for each element. In order to use FEA to predict failure, the true strain at failure must be provided to the software. The failure criterion requires the microscopic compressive and tensile failure strain to fail an element rather than the macroscopic failure strain as written in Section 3.3. Therefore, providing the software with macroscopic strain is not a good indication of the actual failure strain of the material because the fracture strain is a multiple of the macroscopic strain [58].

Failure strain can only be measured experimentally by accurately modeling the final area at the necking region, which is difficult to do in most cases. By modeling a uniaxial tensile specimen and calculating the strain in the necking region when the macroscopic strain reaches the macroscopic failure strain, a realistic failure strain for the material is obtained. This failure strain is used in FEA to predict material fracture in any given geometry under similar loading conditions.

To take this fracture strain into consideration, simulations of uniaxial tension were done for all three magnesium alloys. Material model (MAT_124) was used to account for the tension-compression asymmetry in the material. The fracture strain was computed from the elements in the necking region when the overall macroscopic strain reached the experimental fracture value. Simulations showed that there could be significant differences between the simulated strains at the necking region and the macroscopic failure strain; the strain in the necking zone was 2.4 times higher than the macroscopic failure strain for AM30 (Figure 13).

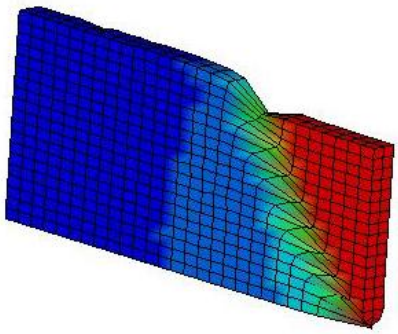

Figure 13: AM30 Failure Strain Simulation Results

Similar numerical simulations for AZ31 and AM60 showed that the failure strain was almost the same as the macroscopic strain at the necking region. However, for all the alloys, the strain at the necking zone was higher than the macroscopic failure strain. Thus, the failure strains employed for the four point bending simulations were higher than the macroscopic failure strains. This approach improves the accuracy of four point bending simulations and discussed in Section 6.3.

Chapter 4
Experiments

Experimental setup for bending and crush experiments is discussed in this chapter. Experimental data from various experiments was used to validate the numerical simulations by comparing experimental stress-strain or force-displacement curves and deformed specimens to the corresponding numerical predictions. Experiments used to validate the model are:

(a) Square Tube Slow and Fast Axial Crush

(b) Four Point Bend Tests

(c) Round Tube Axial Crush

The experimental setup and dimensions for the four point bending and slow and fast axial crush were taken from [9,11,12]. The experimental setup for the round tube with circular cross-section was taken from [1].

4.1 Square Tube Slow and Fast Axial Crush Experiments

Experiments of slow and fast axial crush were performed for AM30, AM60 and AZ31 magnesium square tubes. Slow crush experiments were performed using an end plug at the top end as shown in Figure 14. This was done to keep the specimen in place during the experiment. The aluminum end plugs were between 80-100 mm in length. The experiment was conducted at 50 mm/min. Load and crosshead displacement data was recorded for all magnesium alloys.

Figure 14: Slow Axial Crush Fixture [9]

Fast crush experiments were done using the setup shown in Figure 15. The experiment was done at 6 m/s with the same sized aluminum end plug. Load and crosshead displacement data was recorded for all magnesium alloys. Crosshead displacement is the displacement of the load cell that applies load on the top of the tube.

Figure 15: Fast Axial Crush Fixture [9]

4.2 Four Point Bend Experiments

The experimental setup for four point bend tests had two rollers on the top and two rollers on the bottom. The bottom rollers were fixed while the top rollers applied axial displacement as shown in Figure 16. The experimental setup for the four point bend tests (Figure 16) also had two end plugs on either side of the tube. The lengths of the end plugs were 50 mm and 60 mm on the respective sides. The smaller end plug was used on the side where the crush triggers were located. The bottom rollers were 320 mm apart while the top rollers were 78 mm apart. The diameter of both the rollers was 25 mm and the speed of the top rollers was approximately 12.5 mm/min. To simulate the four point bend test setup, rigid shell elements were used to simulate the rollers and the end plugs (in the tubes). The setup for modeling and the experiment is shown in Figure 14 and Figure 16.

The rollers in the experimental setup are fixed in steel plates which drag the rollers down with them. A possible cause for experimental errors is that during bending, the side walls touched these steel plates and thus, increased compressive stresses in the side walls of the tube.

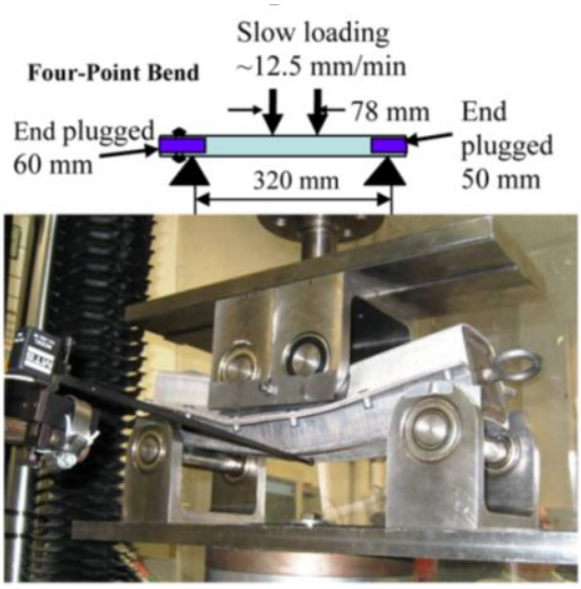

Figure 16: Four Point Bend Test Setup [11]

4.3 Round Tube Axial Crush Experiments

The round tube experiments also involved axial crush experiments. Experiments were done with round tubes with circular cross-section as shown in Figure 17. The experiments were done with AZ31 tubes at a velocity of 7.62 m/s. The tubes were 76.2 mm long with a radius of 25.4 mm and a thickness of 2 mm.

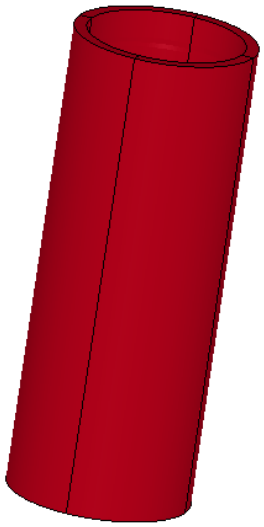

Figure 17: Round Tube with Circular Cross-section

Chapter 5
Finite Element Simulations

This chapter discusses the different parameters used in finite element simulations for this thesis. Round tubes were simulated with different geometrical and material parameters to find the most suitable simulation conditions to match experimental results. Bending and crush simulation parameters are also discussed in detail.

5.1 CAD and Meshing

The square tubes used for axial crush and bending simulations have a near square cross-section as shown in Figure 18. Round tubes with circular cross-section were 76.2 mm long with a radius of 25.4 mm and a thickness of 2 mm. Other details regarding the simulations are mentioned in Section 5.5.

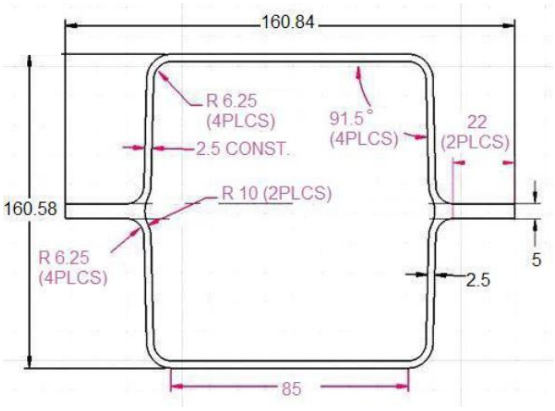

Figure 18: Dimensions of Magnesium Tubes [59]

5.2 Consistent Units

Finite element codes are unit independent as they operate in "normalized" units. For example, SI units for length, time and mass are meters, seconds and kilograms respectively. However, if the model under consideration had a cross-section of only 1 mm x 1 mm, then the stress of 1 Pa would correspond to a force of $1x10^{-6}$ N. This is a very small force and for even smaller samples, the force would be small enough that it can cause round-off errors. These errors accumulate over the length of simulation and produce convergence problems.

The concept of consistent units is used to reduce these errors. Simulations presented in this thesis used kilograms (kg), millimeters (mm) and seconds (s) as units for mass, length and time respectively. Stress, strain, force and displacement quantities were used in this thesis. Other physical quantities like density, young's modulus, velocity etc were also used as inputs for the simulations. The input and the output quantities are affected when standard SI units are not used. For example, in standard SI units, the unit of force is Newtons (N or $kgms^{-2}$) wherem as in our case, the units for forces are milli-newtons (mN). Units of mN for force mean that the forces measured by our simulations are in mN. For example a force of 1000 from the simulations would correspond to 1 mN or 1 N in reality. The explanations are given below.

Units of force, as mentioned before, are N or $kgms^{-2}$. Since the base units are mm, s and kg, the units of force are $Kgmms^{-2}$. To convert this to standard SI units, millimeters have to be converted to meters. The resulting units are given in Equation 8.

$$F = ma = kgmms^{-2} = \frac{kgms^{-2}}{1000} = mN \quad (8)$$

Similarly, the units for stress and density are given in Equation 9 and 10.

$$\sigma = \frac{F}{A} = \frac{kgmms^{-2}}{mm^2} = \frac{\frac{kgms^{-2}}{1000}}{\frac{m^2}{1000000}} = kPa \quad (9)$$

$$\rho = \frac{m}{V} = \frac{kg}{mm^3} = \frac{kg}{\frac{m^3}{1000000000}} = nPa \quad (10)$$

5.3 Round Tube Axial Crush Simulations

Round tube simulations were performed for the magnesium alloy AZ31 for a velocity of 7.62 m/s. The tubes were 76.2 mm long with a radius of 25.4 mm and a thickness of 2 mm. The tubes did not have any crush triggers or end plugs as shown in Figure 19. The round tubes were given a small imperfection near the top to induce buckling as shown in Figure 20.

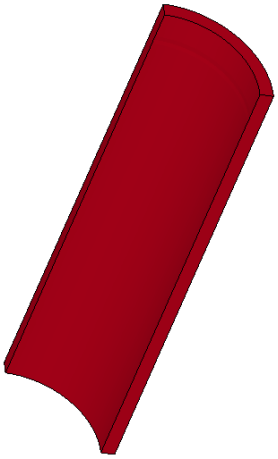

Figure 19: Quarter Round Tube with Circular Cross-Section

Round tube simulations were performed with different geometrical and material parameters to improve the accuracy of the original results. There were a number of different techniques used to implement these changes and are mentioned below. The best results were achieved by a combination of all the parameters.

5.3.1 Imperfections

The round tube presented in Figure 21 has a small imperfection at the top to initiate buckling in the sample (Figure 20). Without the initial imperfection, the sample would not buckle as it would in the real experiment. This technique is used in finite elements in many cases where deformation of some kind is induced in the sample to predict accurate results. The location of the imperfection was moved along the tube and the best results were found when the imperfection was near the top surface as shown in Figure 20.

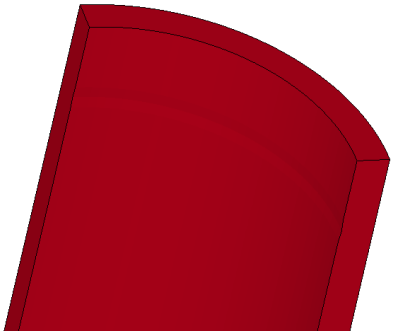

Figure 20: Imperfection in Round Tube Simulations

5.3.2 Boundary Conditions

In all the simulations, only a quarter of the actual specimens were modeled since symmetry assumptions were applicable. Thus, the conditions listed below were all satisfied by assuming quarter symmetry (Figure 21).

(a) Isotropic material

(b) Symmetric loading

(c) Boundary conditions

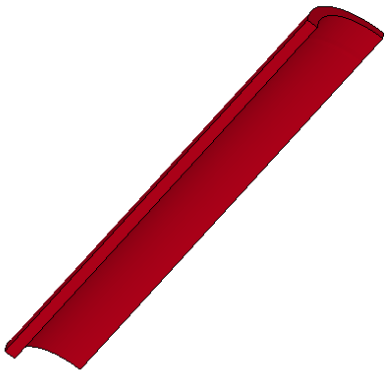

Figure 21: Round Tube with Quarter Symmetry

Boundary conditions were applied to the top and bottom surface of the model. The top surface was free to move in the vertical direction and was constrained in all the other directions. It was also constricted in moments in all directions since the top of the tube was usually held tight since these experiments were performed at high speeds.

The bottom surface took the impact from the wall. To simulate this, no movement was assumed in the z-direction (Figure 22). The tube, however, was free to move in the x and the y-directions.

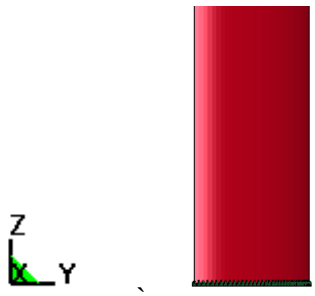

Figure 22: Bottom Surface for Round Tube Axial Crush Simulations

The assumption of no motion in x and y-directions corresponds to experiments that involve slip when the tube hits the wall. However, this was not necessarily true in this case. Therefore, simulations were performed assuming motion in both x and y-directions.

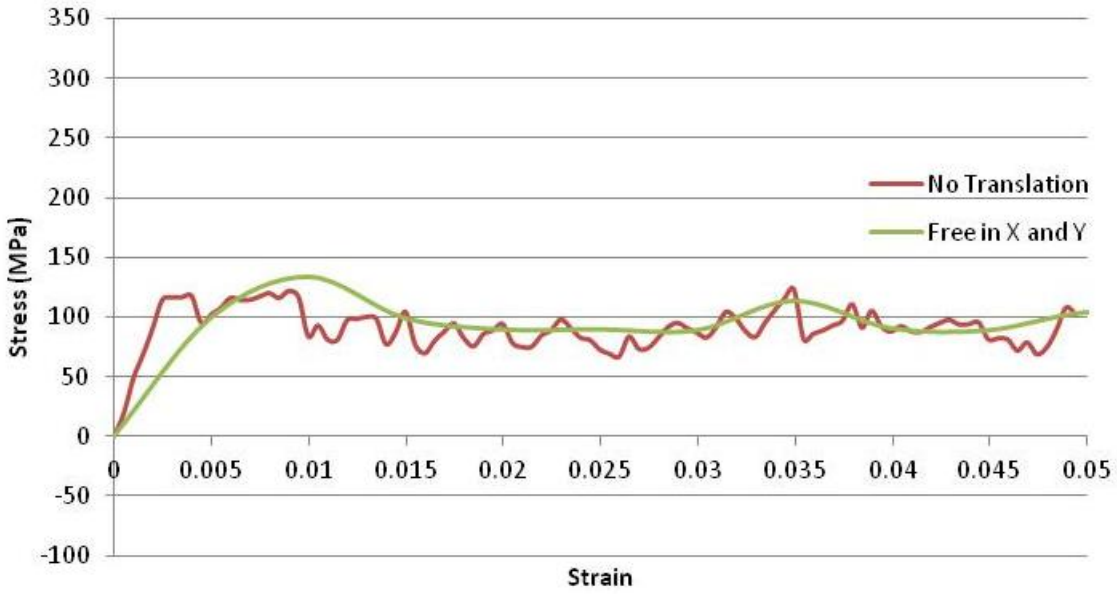

Figure 23: Stress Strain Curves with Different Boundary Conditions

For all round tube simulations there were no moments in any direction. The results for both cases, as discussed above, are given in Figure 23. It is shown that constricting the translation in all directions predicted lower initial forces, but the initial stress on small strains was considerably more than in the real experiment. Keeping the bottom surface free in the x and y-directions provided improved predictions, which were closer to the real experiment.

5.3.3 Load Curve

Loads were applied on the top surface of the round tubes with circular cross-section (Figure 19). The nodes on the upper surface were given an initial velocity until the tube was crushed, as shown in Figure 24. The load curve is shown in Figure 25.

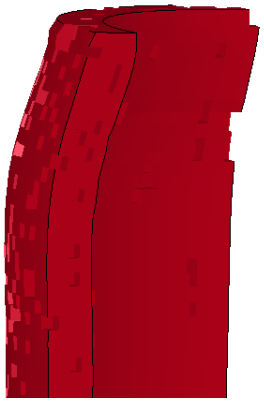

Figure 24: Crushed Tube

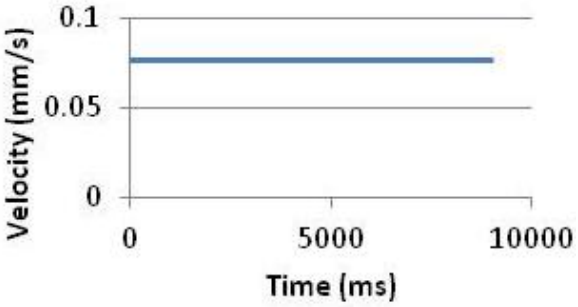

Figure 25: Simple Load Curve

Another load curve was also applied to the simulations (Figure 26). This load curve ramps the velocity slowly, thus decreasing the initial acceleration experienced by the sample. The slow ramp in velocity removed the effect of high impact caused by having a sudden increase in velocity. The difference between the two assumptions was in the initial acceleration. High acceleration in the beginning of the simulation initially produced a spike in force, which may not represent what happened in the actual experiment.

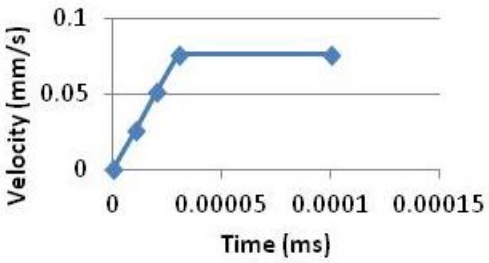

Figure 26: Modified Load Curve

Thus, the new load curve was employed in the simulations for the round tube. The results with different load paths were compared as shown in Figure 27. The results show that the modified load path yields a high stress on a very low strain value which does not match the actual experiment. Therefore, it is concluded that the modified load curve did not predict the experiment well because the initial experiment involved high impact loading, which was clearly predicted by the initial load curve (Figure 25).

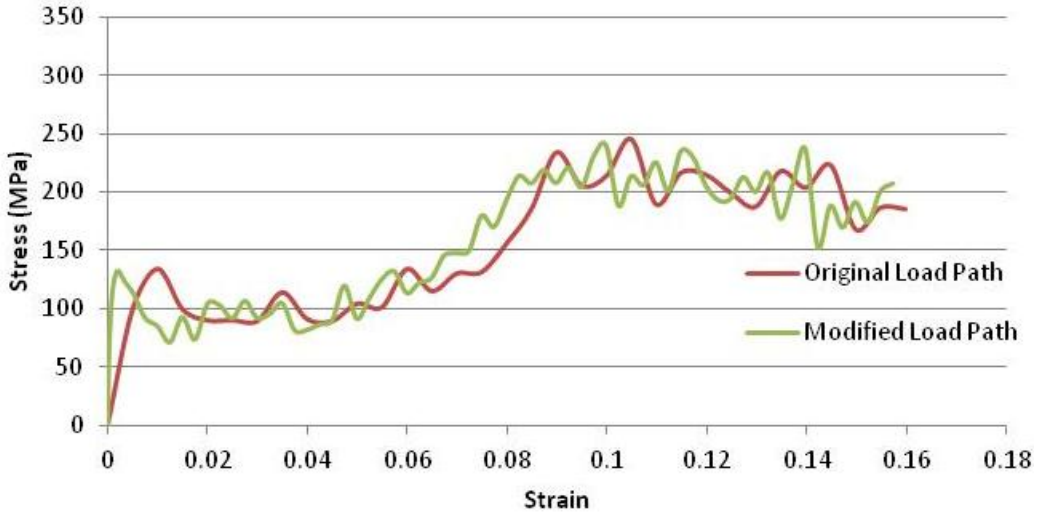

Figure 27: Stress Strain Curve with Different Load Paths

5.3.4 Time Scaling

In finite elements, one of the biggest concerns is the execution time of the simulations. If a simulation is run in real time, the time it takes for a finite element code to solve the problem may take a lot more CPU time. To solve this problem, time scaling was employed. To speed-up the CPU times of the simulations, the speed of impact was increased. This reduced the total time of simulation and hence took less time to get results. The results were compared with varying speeds to confirm if the results properly converged.

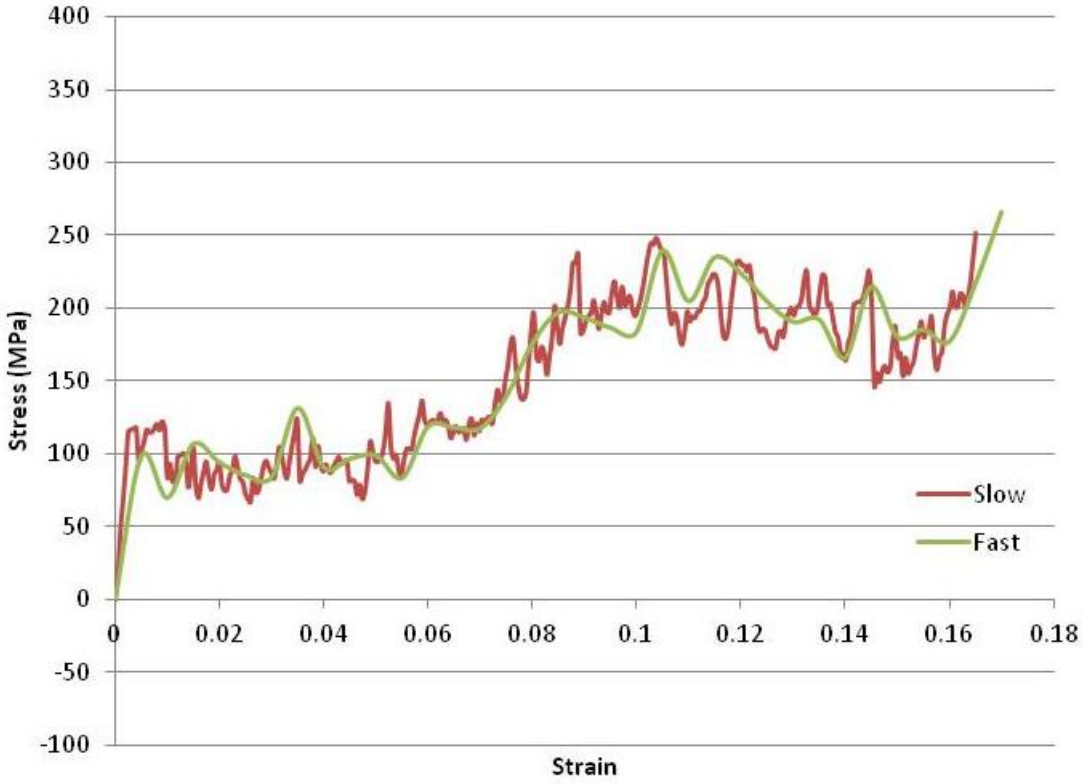

Figure 28: Stress Strain Curve Time Scaling

Figure 28 shows two simulations with different time scaling. There is a difference of a factor of 10 in the applied velocity between the fast and the slow simulations. The stress-strain paths for both the simulations were pretty close and hence do not contribute a considerable difference in the actual results. Therefore, it is concluded that time scaling the simulations do not affect the results significantly.

5.3.5 Hourglass

A common problem in finite element simulations is that an element or a number of elements undergo a zero energy state [56]. These states are called hourglass. The direct impact of this state results in oscillatory response of the simulation. Figure 29 shows two curves with oscillatory and non-oscillatory behavior. In some cases, these oscillations have large amplitudes and therefore have to be addressed. In the simulations presented in this research, hourglass control was used to address these zero states. Another advantage of hourglass is that it allows damping (Section 5.3.6) of the system to reduce the oscillations in the simulation response.

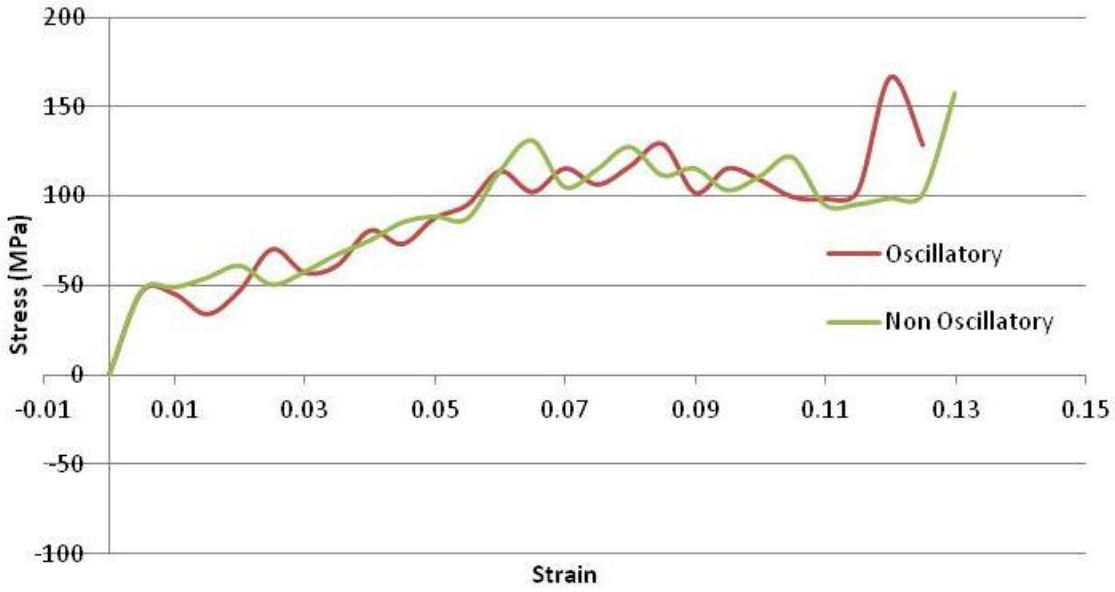

Figure 29: Stress Strain Curve showing Oscillatory and Non Oscillatory Curves

5.3.6 Damping

Damping is another parameter used in finite elements to improve results. Damping is used to reduce the oscillations in the system which might result from zero states or the setup in the simulation. Oscillations in the simulation are also caused due to time and mass scaling of the simulation. In this research, damping was used to reduce the oscillatory response in the predictions as shown in Figure 29. It is possible to use hourglass for the same purposes; however, damping with hourglass provided the best results, as shown in Figure 29.

5.4 Square Tube Crush Simulations

In this section, numerical simulations of axial crush tests are presented. Crush simulations were performed with an imposed axial displacement at one end of the tube while the other end was fixed. Furthermore, square tubes of magnesium alloys, AM60, AM30 and AZ31, all have crush triggers for crush simulations. There were some differences in the magnesium tubes for different alloys as shown in Figure 30 and Figure 31.

Figure 30: AM60 and AZ31 Crush Model

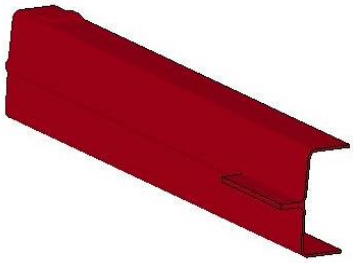

Figure 31: AM30 Crush Model

Square tubes were simulated for half symmetry as the boundary conditions; loading and material geometrical properties were symmetric. Square tubes have flanges that go from the top to bottom ends of the tube and have crush triggers on one side as shown in Figure 30 and 31. Solid quadrilateral elements were used for meshing the magnesium tubes with multiple elements across the thickness to simulate material failure. It is noted that shell elements can also simulate material failure but since it is not possible to have multiple elements in the thickness, they were not used in the simulations. Solid elements provide a better understanding of failure by having multiple elements in the through- thickness direction.

Boundary conditions for the square tubes under bending and axial crush were imposed on the top, bottom and side nodes. Since velocity was applied on the top surface, the top surface was only allowed to move in the z-direction (Figure 32). All moments were also constrained. The bottom surface was fixed and was constrained in all directions and moments. Symmetry boundary conditions were applied on the tube walls parallel to the yz plane (Figure 32). The walls were constrained for motion in x-direction and moments in y and z-direction were considered equal to zero.

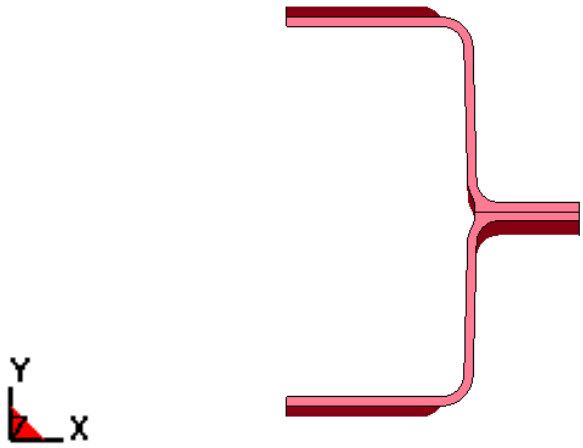

Figure 32: Boundary Conditions for Axial Crush Simulations for Square Tubes

The experimental setup for the round tubes (Figure 19) did not have any end plugs in the simulations but the setup for the square tubes (Figure 30 and Figure 31) had an end plug. The lengths of the end plugs were between 80-100 mm. In the numerical analyses, rigid shell elements were used to simulate the end plugs (in the tubes) and the compression plates.

5.5 Bending Simulations

In this section, numerical simulations of square tubes under bending are presented. Commercial software, Hypermesh, was used to mesh the models. It is noted that there were some differences between the tubes for each alloy. However, for the purpose of the simulations, the same square tube was used for all three alloys as shown in Figure 33. The model for the bending simulations was drawn for half symmetry (Figure 33) like the four point bend problems with the same type of loading and boundary conditions as shown in Section 5.4. The tube has flanges that go from the top end to the bottom end of the tube. The tube also has crush triggers on one side, as shown in Figure 34. Solid quadrilateral elements were used for meshing the magnesium tubes with multiple elements across the thickness to simulate material failure. A higher mesh density was used near the top rollers, as this was the expected area of failure. Due to reasons explained in section 4.3, solid elements were employed in the simulations.

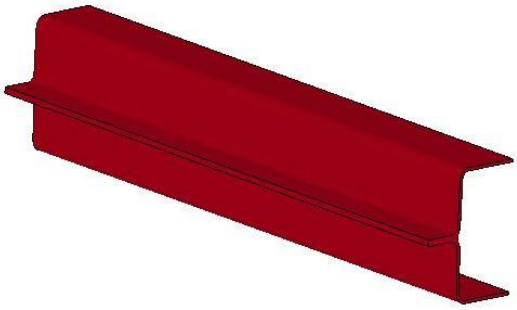

Figure 33: Square Bending Tube

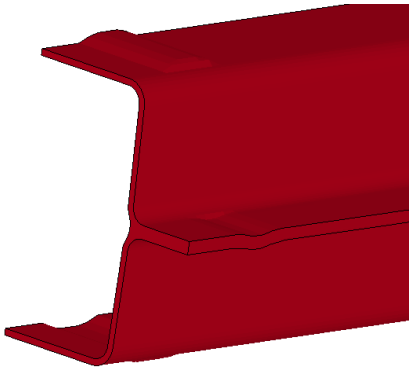

Figure 34: Square Tube with Crush Triggers

Bending simulations were performed by applying axial displacements on the top surface of the tube walls. The bottom rollers were fixed and there were also end plugs at each end. Figure 35 shows the setup of the numerical model employed in all the four point bending simulations.

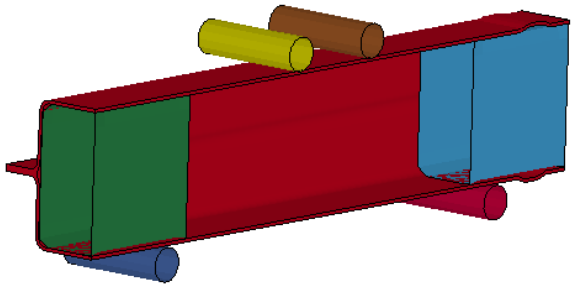

Figure 35: Four Point Bend Test Simulation Setup

Chapter 6
Results and Discussion

In this chapter the stress-strain results from experiments and simulations are presented for the AZ31 round tubes. Experimental and simulated force-displacement results for AM30, AM60 and AZ31 are also presented for axial crush and bending conditions. Simulated results are also compared for geometrical similarities in the deformed specimens for the three magnesium alloys. The results of using rivets and failure strain in some simulations are also presented.

6.1 Round Tubes Axial Crush

The failure criterion was initially developed for round tubes with circular cross-section. The results are presented in [1]. The results presented in this thesis demonstrate improved accuracy (in terms of force-displacement curves and deformed specimens) due to modifications in the failure criterion and parametric studies (discussed in detail in Section 5.3). Axial crush experiments are usually compared by investigating the force-displacement curves. The area under the force-displacement curve represents the energy absorbed by the material before failure. A larger area corresponds to a material that can absorb a lot of energy before failure. For crashworthiness applications, a material that can absorb the maximum energy possible is desired. However, only stress-strain data was available for the round tube experiments. Therefore, the experimental stress-strain was plotted against simulation stress-strain data. The area under the stress-strain curve gives the energy absorbed per unit volume and can therefore be used for crashworthiness applications.

Figure 36 presents a comparison between the initial results of the FE simulations and experiments. It is seen that the simulation accurately follows the experimental trends. The initial stress jump in the simulation, however, was very large compared to the experiment. The maximum initial stress from the experiment was 90 MPa, while the simulation predicted an initial stress of 140 MPa. The peak force was also accurately predicted by the simulation. Experiment 1 shows a peak force of 220 MPa while the simulation predicted a peak force of 235 MPa. These results were further improved with the parametric study presented in Section 5.3.

Figure 37 shows the final predictions for the round tube where the results show improvement compared to the initial results. The initial peak stress decreased from 140 MPa to 110 MPa while keeping the initial slope the same. The peak force did not change considerably, compared to the initial

FE results. The final FE results give a peak force of 225 MPa compared to the experimental peak force of 220 MPa.

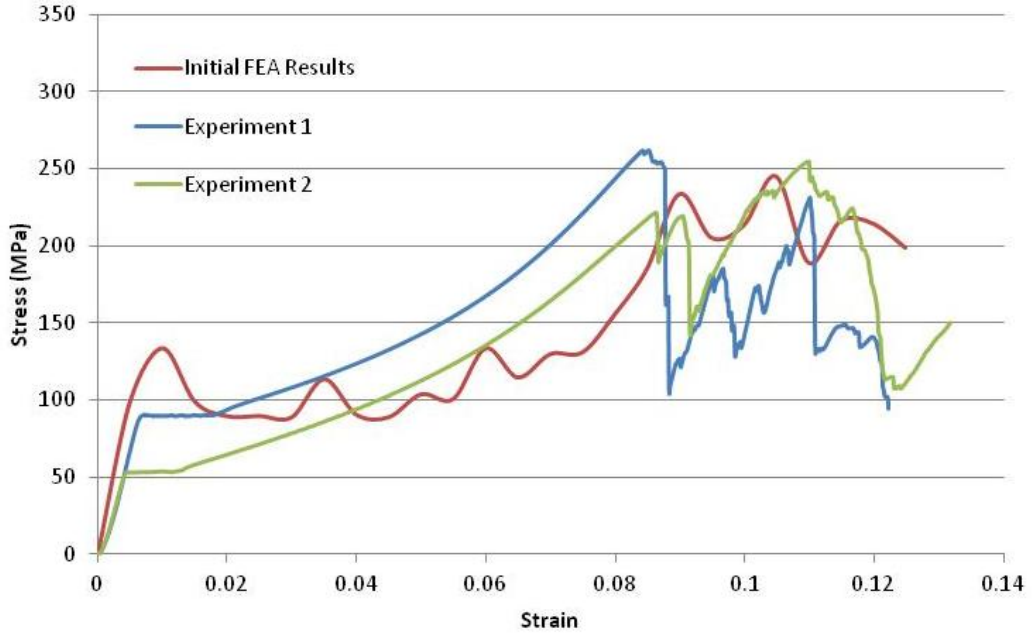

Figure 36: Experimental and Simulated Stress Strain Comparison for Axial Crush of AZ31 Round Tubes (Initial FEA Results)

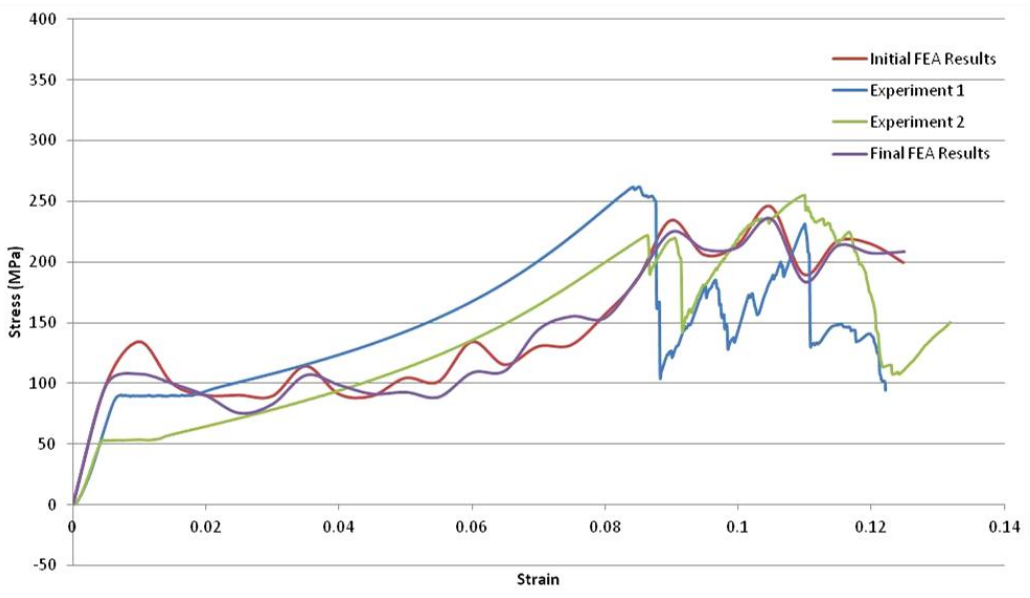

Figure 37: Experimental and Simulated Stress Strain Comparison for Axial Crush of AZ31 Round Tubes (Final FE Result)

6.2 Slow and Fast Axial Crush

The failure criterion employed in this research was initially developed for axial crush [1]. This research demonstrates the applicability of the criterion for various axial crush scenarios. Predictions with the failure criterion were validated by comparing numerical simulations to the corresponding experimental observations (force-displacement graphs and deformed specimens). The simulation results show that the model accurately predicts the failure point for crush simulations as shown in Figure 38-43. In some cases, the experimental results were not available and only the simulation results are presented.

6.2.1 Comparisons of Deformed Specimens

In this section, the deformed specimens from experiments are compared to the predicted ones. These comparisons (failure locations, geometrical changes) were necessary to investigate the predictive capability of the failure criterion.

6.2.1.1 AZ31 Slow and Fast Axial Crush

Prediction of fast axial crush simulations with experimental results is shown in Figure 38a and b respectively. Simulation of AZ31 slow crush (Figure 38) accurately predicts the locations of failure when compared to experiments. The simulation also captures the bulges near the crush trigger and failure points. Figure 39 shows the simulated results for fast crush for AZ31. Unfortunately, there were no experimental observations available to compare with the simulations.

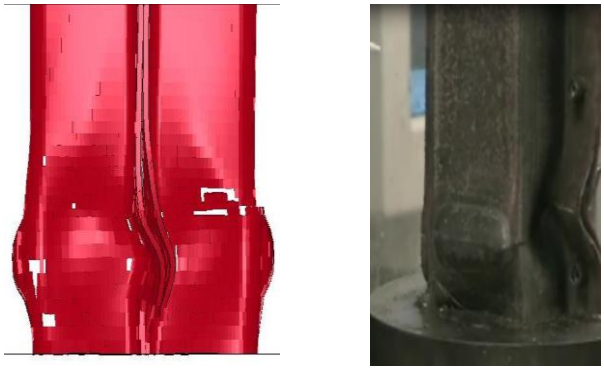

(a) **(b)**

Figure 38: Experimental and Simulated Failure Prediction for AZ31 (Slow Crush)

Figure 39: AZ31 Simulation Prediction Results (Fast Crush)

6.2.1.2 AM30 Slow and Fast Axial Crush

The predicted deformed meshes from the slow crush simulations as well as the corresponding experiments for AM30 are presented in Figure 40a and b respectively. The simulation correctly predicts the bulges in the AM30 tube (caused by large deformations). Figure 41a and b show the fast crush simulation and experimental results for AM30 respectively. The simulation predicts the failure areas near the crush triggers along with the large deformation bulges.

(a) **(b)**

Figure 40: Experimental and Simulated Failure Prediction for AM 30 (Slow Crush)

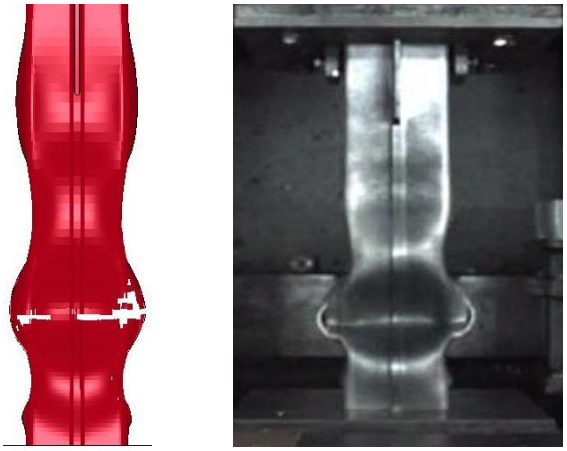

(a) **(b)**

Figure 41**: Experimental and Simulated Failure Prediction for AM 30 (Fast Crush)**

6.2.1.3 AM60 Slow and Fast Axial Crush

The experimental and predicted deformed specimens during the slow axial crush of magnesium alloy AM60 are presented in Figure 42a and b respectively. The predicted deformed specimen demonstrates the capability of the model to accurately predict the failure area in the tube. Figure 43 shows the simulated deformed specimen during fast axial crush of the magnesium alloy, AM60. Unfortunately, there weren't any experimental pictures available for this alloy under fast axial crush experiments.

(a) **(b)**

Figure 42: Experimental and Simulated Failure Prediction for AM 60 (Slow Crush)

Figure 43: AM60 Simulation Prediction Results (Fast Crush)

6.2.2 Comparison of Force-Displacement Curves

The predicted load-displacement curves were also compared with experiments for fast axial crush tests (for all three alloys). The curves for the three alloys show a lot of discrepancy in the initial stages but after around 15 mm displacement, the curves matched the experimental results closely in most cases.

The discrepancy in the initial stages of the results is possibly due to experimental errors. It is very likely that the sensors used to track the force-displacement data were not able to record the sharp peaks in force. Another cause for discrepancies is possibly due to incomplete information about the experimental setup. Factors like load curves, weight of load cell, friction with the rigid wall on impact and location of sensors played an important role in capturing the results. Furthermore, the weight of the experimental setup accounts for momentum that is transferred to the system on impact. This momentum affected the force recorded due to the acceleration caused by the mass. Finally, other factors like elastic wave propagation in the sample affected the recorded force by the load cell as demonstrated in [60]. Therefore, all the results in this section are normalized by the maximum force due to the reasons mentioned above.

6.2.2.1 AZ31 Slow and Fast Axial Crush

Simulations show that the numerical model predicted the failure point and the maximum force during the slow axial crush test of AZ31 (Figure 44). The initial trend of the experimental and simulated curves is similar for the slow crush tests. AZ31 fast axial crush simulations predicted the maximum

load with reasonable accuracy considering the experimental issues explained above. AZ31 fast axial crush simulations also predict the trend after 20 mm displacement as shown in Figure 45.

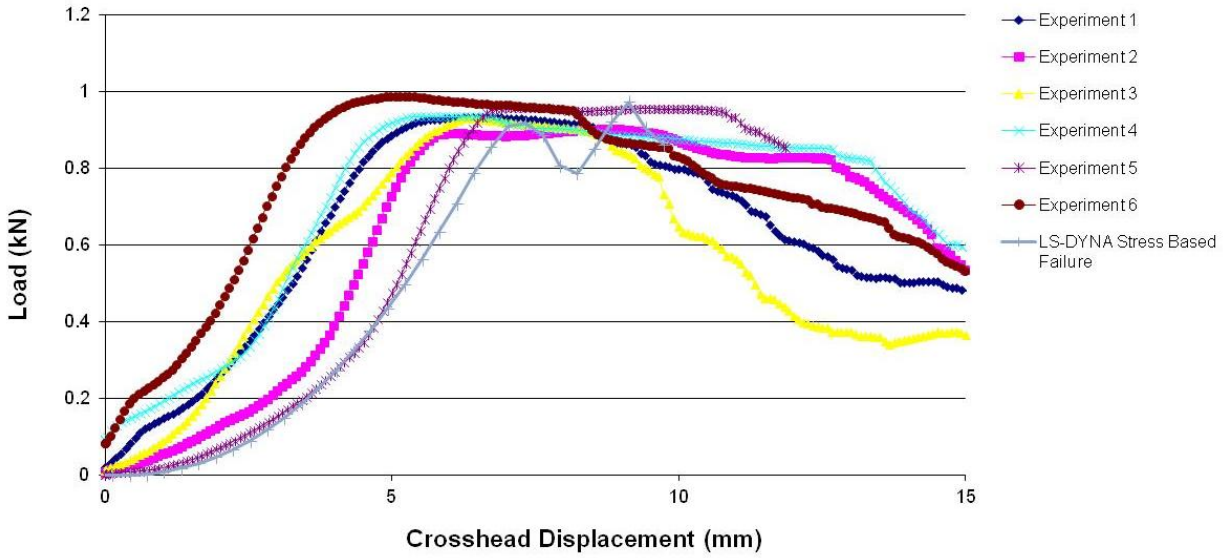

Figure 44: AZ31 Slow Crush Simulation and Experiment

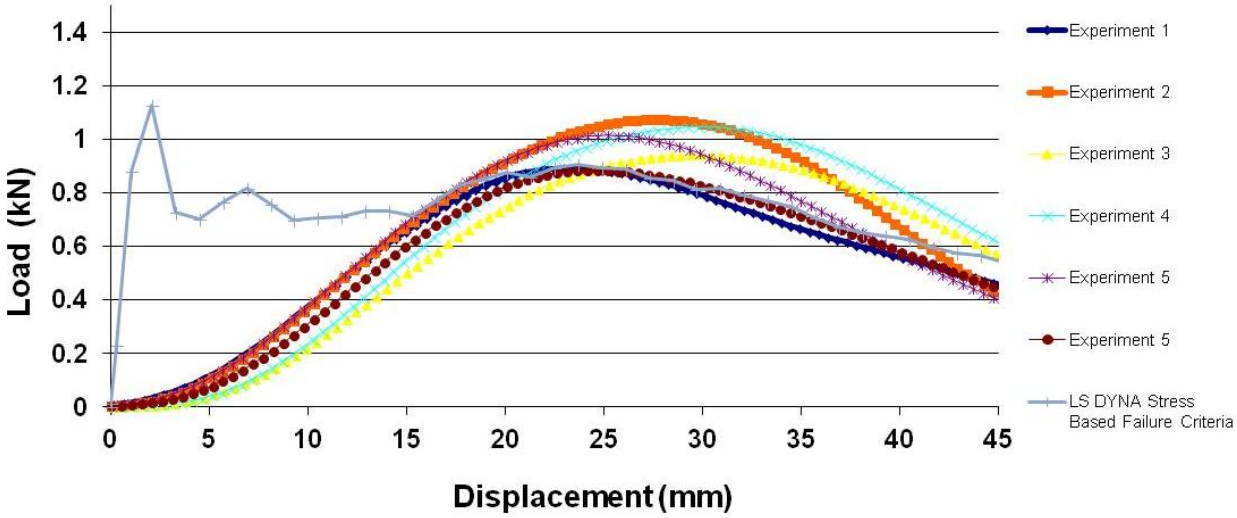

Figure 45: AZ31 Fast Crush Simulation and Experiment

6.2.2.2 AM30 Slow and Fast Axial Crush

Simulations of AM30 slow axial crush test show that the trends and maximum force were predicted with close accuracy, as shown in Figure 46. This figure also shows results from LS-DYNA without the failure criterion. LS-DYNA predictions without the new failure criterion do not match the experimental trends. Figure 47 shows the simulated and experimental results for AM30 fast axial crush test. The experimental trends do not match the simulated trends for the fast axial crush test. As mentioned earlier, this difference in simulated results is possibly due to low resolution sensors employed in the experiments as explained above.

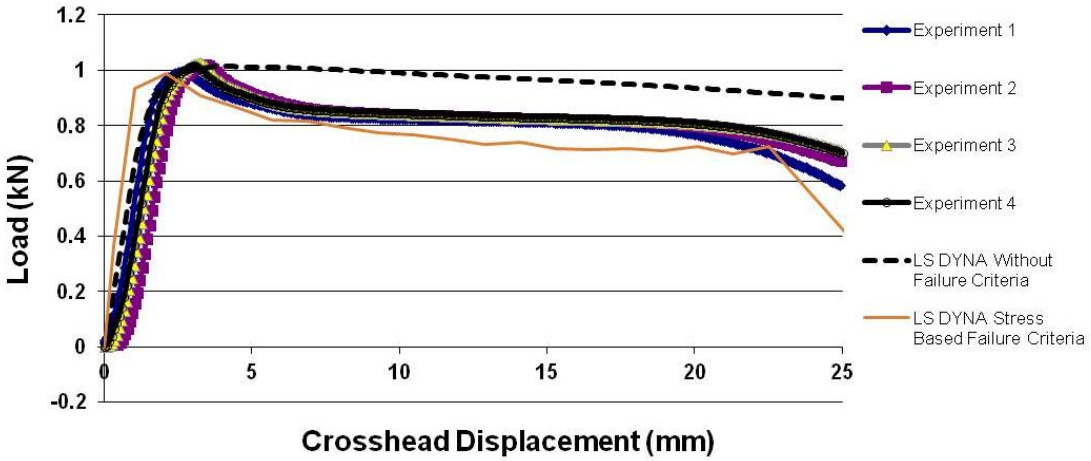

Figure 46: AM30 Slow Crush Simulation and Experiment

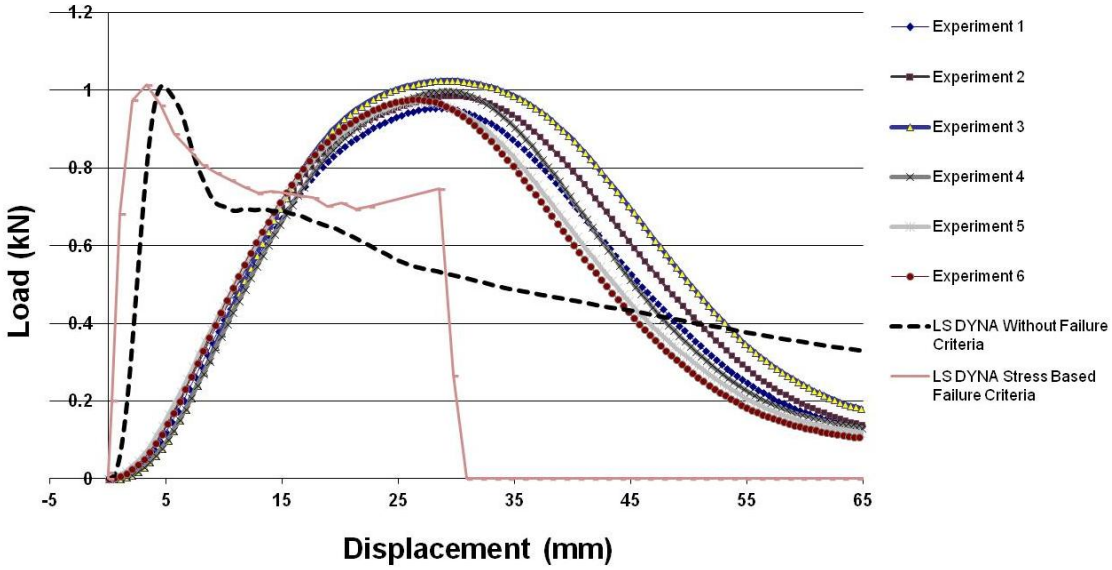

Figure 47: AM30 Fast Crush Simulation and Experiment

6.2.2.3 AM60 Slow and Fast Axial Crush

Simulations show that the numerical model accurately predicted the load-displacement curve as well as the maximum force during the axial slow crush test of the magnesium alloy, AM60 (Figure 48). The trends and maximum force were also predicted accurately for axial fast crush tests (Figure 49). The difference in the fast crush tests is mainly due to the anisotropy of the material along with some problems in the experimentation and experimental data provided. Once again, the errors are possibly due to low resolution sensors used to capture the force-displacement data.

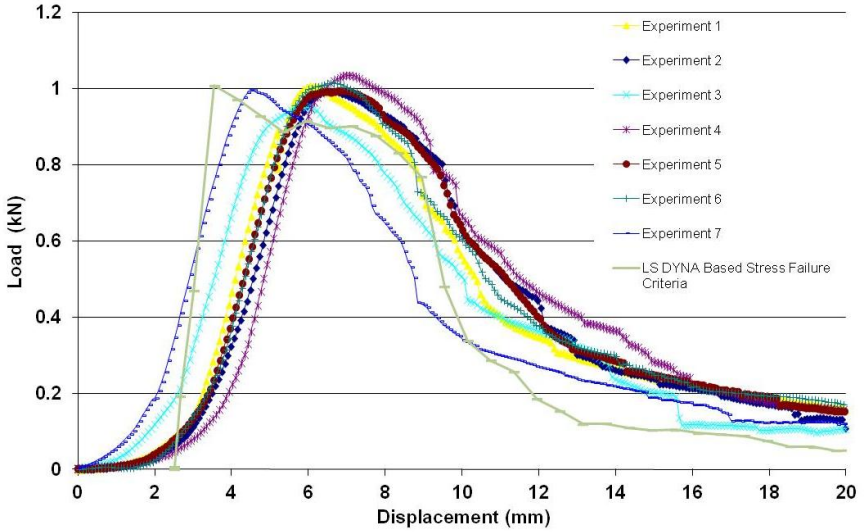

Figure 48: AM60 Slow Crush Simulation and Experiment

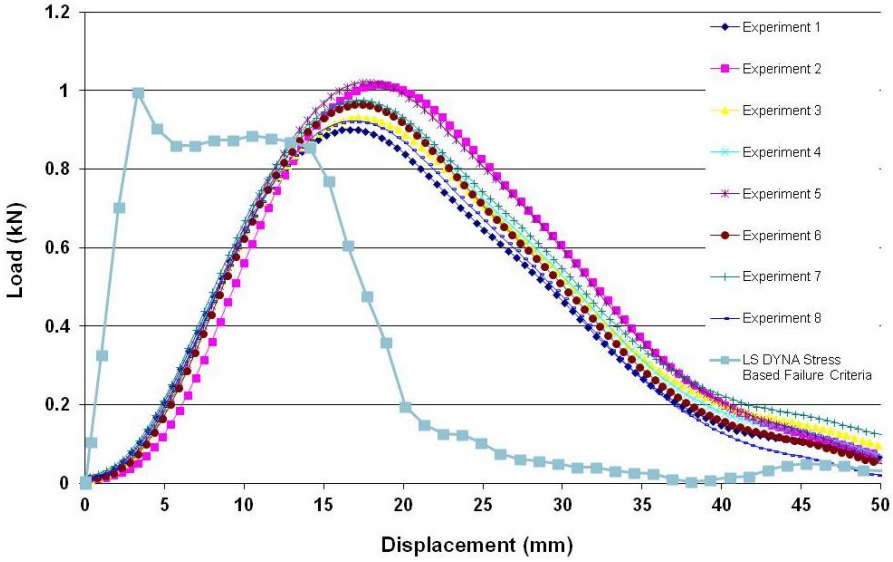

Figure 49: AM60 Fast Crush Simulation and Experiment

6.3 Four Point Bend Test

The failure criterion employed so far in this thesis was initially created for axial crush [1]. The results presented in this thesis show that the criterion is also applicable for four point bending tests. The simulation results show that the model predicts the failure point for bending simulations with good accuracy. In the cases where the experimental results were not available, only the simulation results are presented.

Simulations with the failure criterion are compared to experimental results (force-displacement curves as well as deformed specimens) to validate the model. Since the failure criterion is based on element erosion, the failure in the experiments and simulations is easily comparable.

6.3.1 Deformed Specimens

In this section the deformed specimens predicted by the numerical model are compared to experimental observations during the four point bending tests.

6.3.1.1 AZ31 Four Point Bend Test

Simulations of four point bend tests of AZ31 (Figure 50a and b) clearly demonstrate that the model can accurately predict experimental observations such as the locations where the tube fails under the load on the top part of the beam. It also shows the top roller imprints and the bulge between the top rollers on the top wall. Furthermore, simulation predicted the bulge on the side-walls of the tube.

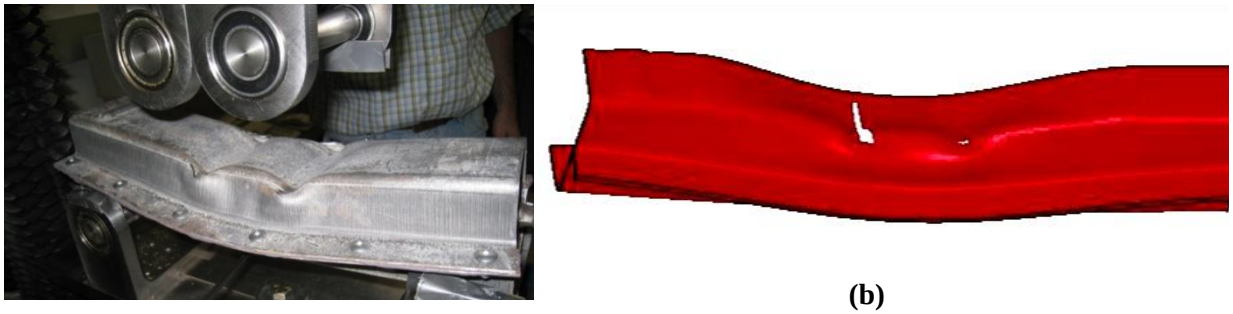

(a) **(b)**

Figure 50: Experimental and Simulated Failure Prediction for AZ31 (Four Point Bend Test)

6.3.1.2 AM30 Four Point Bend Test

Simulations of four point bend tests of AM30 (Figure 51) show the failure points at the locations where the rollers impacted the tube. The tube also bulged between the rollers on the top and side-walls (due to compression). There were no experimental pictures available to confirm this phenomenon. However the experimental and simulated force-displacement curves are presented in Section 5.3.2.

Figure 51: AM30 Simulation Prediction Results (Four Point Bend Test)

6.3.1.3 AM60 Four Point Bend Test

Simulations of four point bend tests of AM60 (Figure 52a and b) show locations of failure for the tube that are very similar to the experimental locations of failure. The tube presents a bulge between the rollers on the top wall. However, the bulge on the side-walls is less prominent compared to the AM30 and AZ31 square tubes.

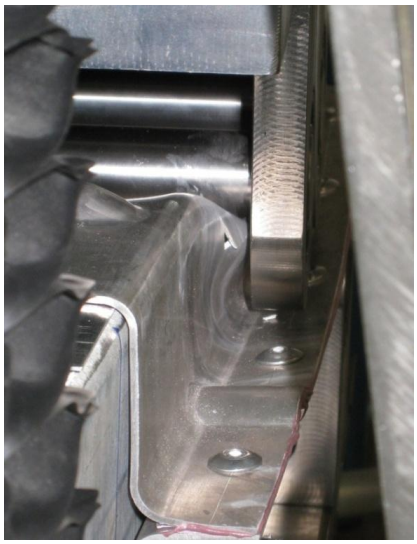

(a)

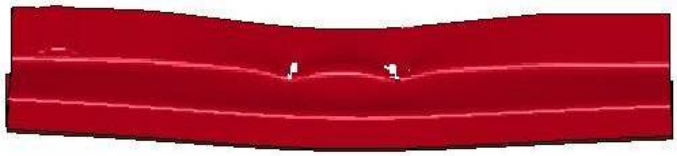

(b)

Figure 52: Experimental and Simulated Failure Prediction for AM 60 (Four Point Bend Test)

6.3.2 Comparisons of Force-Displacement Curves

In this section the load-displacement curves during four point bending simulations were plotted and compared with experimental results. Load-crosshead displacement curves are important tools and are used to find the crashworthiness of metals [61]. Square tubes are used for crashworthiness simulations since they exhibit energy dissipation mechanisms [61]. The area under the load-crosshead displacement curve represents the energy absorbed by the tube and the results obtained from these simulations help engineers predict the crashworthiness of materials. Thus, accurate simulations help engineers to implement materials into real life applications to minimize damage caused under crash conditions to improve safety.

6.3.2.1 AZ31 Four Point Bend Test

The four point bending test simulation for AZ31 (Figure 53) accurately predicts the relatively complicated trend, the maximum force and the location of failure. The peak load in the experimental setup was roughly 28 kN force at 31 mm displacement. The simulation results predicted the peak load at 35 mm displacement and 29 kN force.

As AZ31 tubes were joined with rivets, simulations with rivets were done to improve the results (Figure 54). Rigid rivets were used in the simulations, since detailed rivet specifications were not available. However, the number of rivets and their locations were known. The predicted load-displacement curve with rivets is presented in Figure 54.

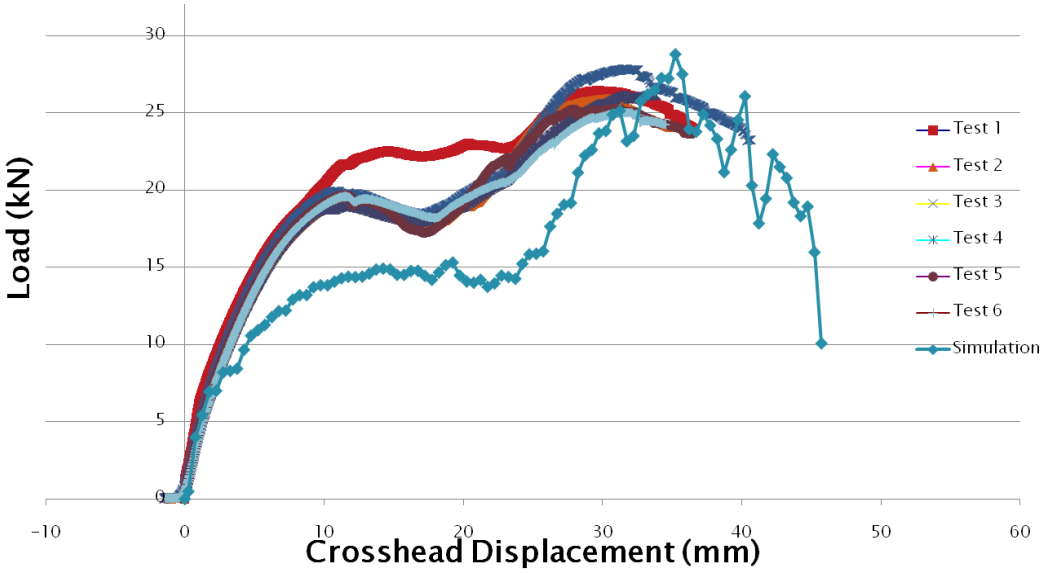

Figure 53: AZ31 Four Point Bend Experimental and Simulation Results

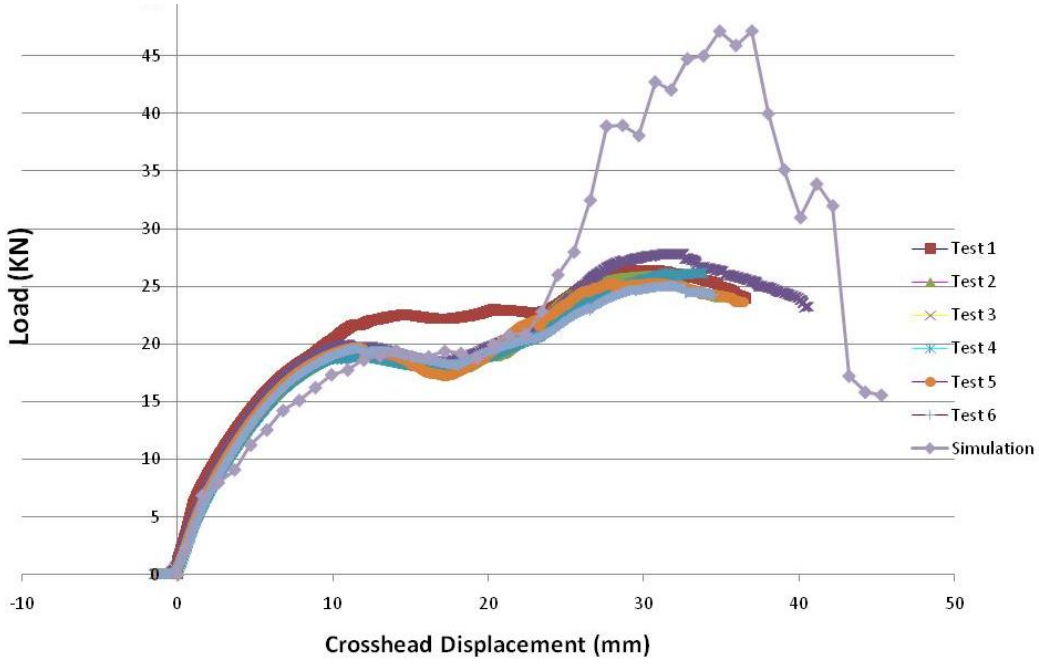

Figure 54: AZ31 Four Point Experimental and Simulation Results with Rigid Rivets

Due to the assumption of rigid rivets, the results show that the initial trend was accurately predicted up to a displacement of 25 mm. The sudden rise in force after 25 mm displacement was due to the fact that the tube was crushed in the simulation. The tube has crushed around 25 mm in the simulation due to the rigid rivets (Figure 55). Rigid rivets do not break and hence, restrict separation between the two halves of the tube, resulting in high forces (Figure 54). In the actual experiments, the rivets deformed which is contrary to the assumptions made in the numerical analyses.

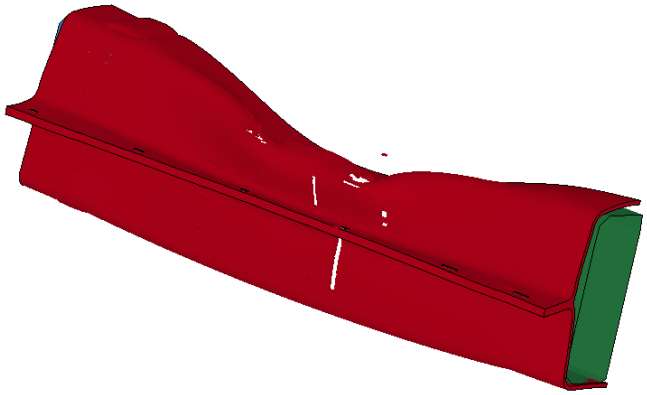

Figure 55 AZ31 Four Point Bend Test Crushed Tube with Rivets

In the initial stages, the experimental curve shows a sudden increase around a displacement of 11 mm and a force of 19 kN while the simulation shows the same peak around 14 mm displacement and 19 kN force. Thus it can be concluded that the introduction of rivets in the simulation produced better results for the initial stages of deformation. A better representation of the results was achieved by combining the original simulation with the simulation including the rivets (Figure 56). This was necessary since the simulation results with rivets do not represent the experimental conditions after a displacement of 25 mm, as explained above. Thus, in Figure 56, the first part of the curve is from the simulation with rivets (Figure 54) and the second part of the curve is from the original simulation (Figure 53). It is shown that the force trends match very well with the experiments.

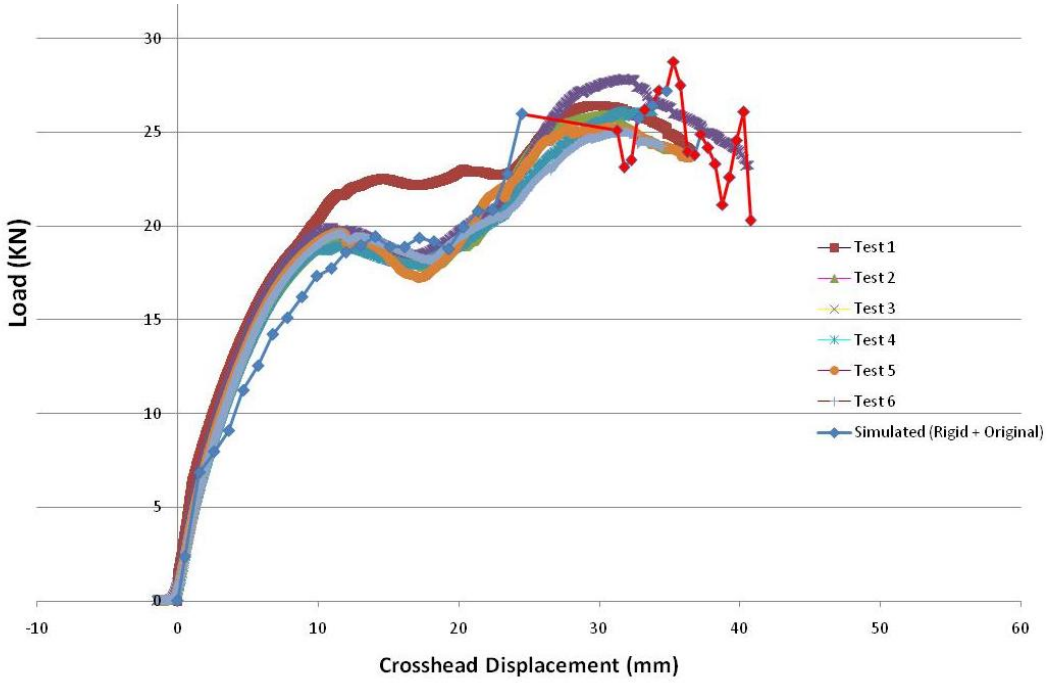

Figure 56: AZ31 Four Point Experimental and Simulation Results (Rigid Rivets + Original)

A comparison between the AZ31 four point bend predictions from this research (Figure 57) with similar predictions presented in [12], demonstrates significant differences between the predictive capabilities of the two different models. The model employed in [12] was not able to predict the dip in force of roughly 15 mm displacement and it also over predicted the force in that region. In contrast, the simulation with rivets (Figure 54) accurately predicts the material behavior in that region.

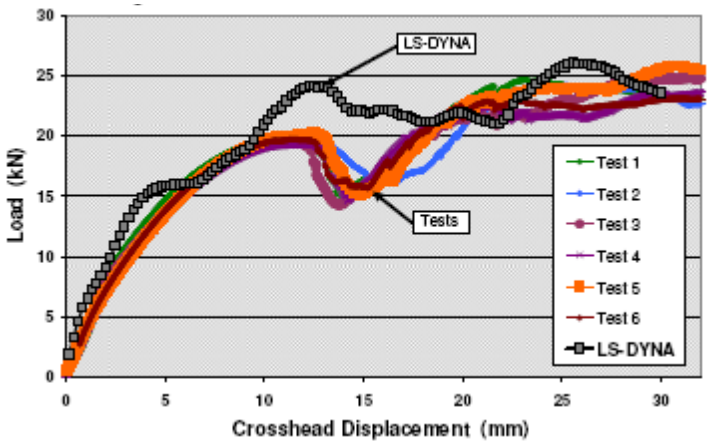

Figure 57: AZ31 Four Point Bend Test Experimental and Simulated Results as Presented by Wagner et al [12]

6.3.2.2 AM30 Four Point Bend Test

Simulations of four point bend tests for AM30 (Figure 58) predicted the maximum force and the overall trend of the force-displacement curve accurately. It is noted that the rise in force at around 15 mm displacement is mainly due to the rigid behavior of the top rollers used in the four point bend test. At 15 mm, the tube started to fail near the rollers. The removed elements gave rise to a high concentration of bending stress which resulted in higher forces on the top rollers. The force decreased after 15 mm as elements failed at other locations. Element deletion at other locations on the tube spread the stress concentration thus resulting in a reduction of force experienced by the top rollers.

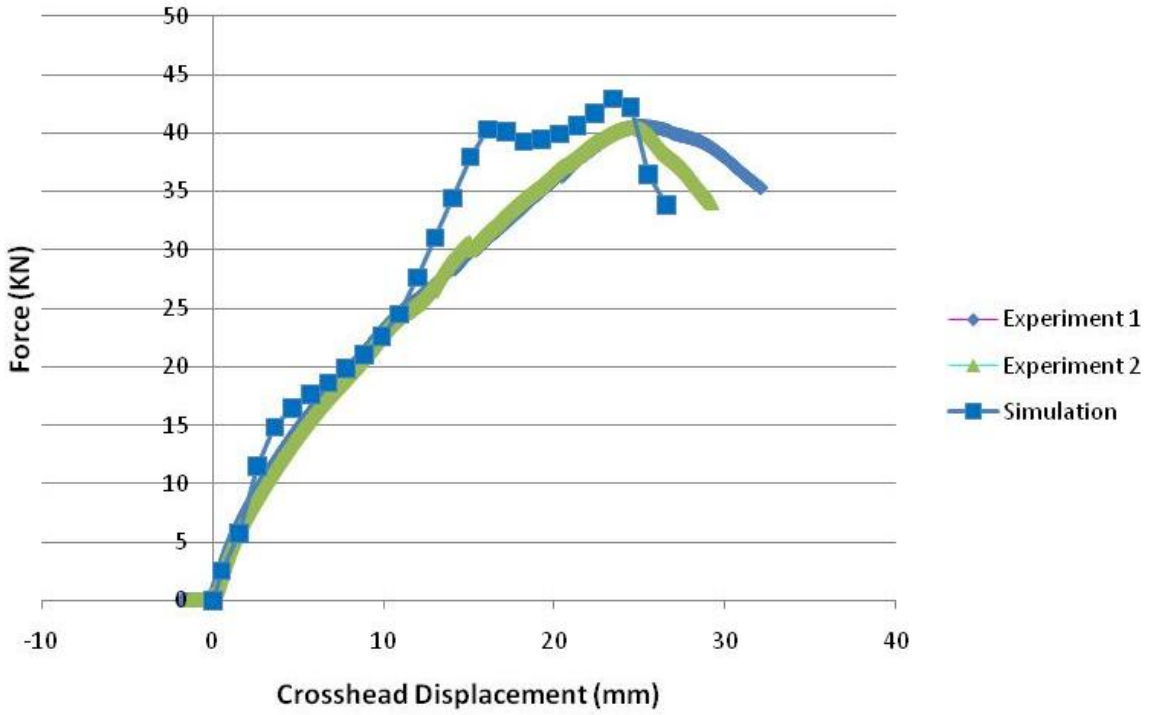

Figure 58: AM30 Four Point Experimental and Simulation Results

As mentioned earlier in Section 3.3, AM30 fracture strain at neck was 2.4 times higher than the macroscopic fracture strain. Figure 58 shows the results after the fracture strain in the neck area (during uniaxial tension) was incorporated. Furthermore, predictions where the overall macroscopic failure strain (in uniaxial tension) was employed in the simulations are presented in Figure 59. The trends clearly show the effect of employing the fracture strain (in the neck area) on the simulation. The peak load without the fracture strain was around 25 kN at 23 mm displacement while the actual experimental load at the same crosshead displacement was around 40 kN. After the incorporation of the new fracture strain factor, the peak load in the simulation was around 42 kN and the experimental

peak load was 40 kN (Figure 58). This approach improved the accuracy of the predictions by approximately 30%.

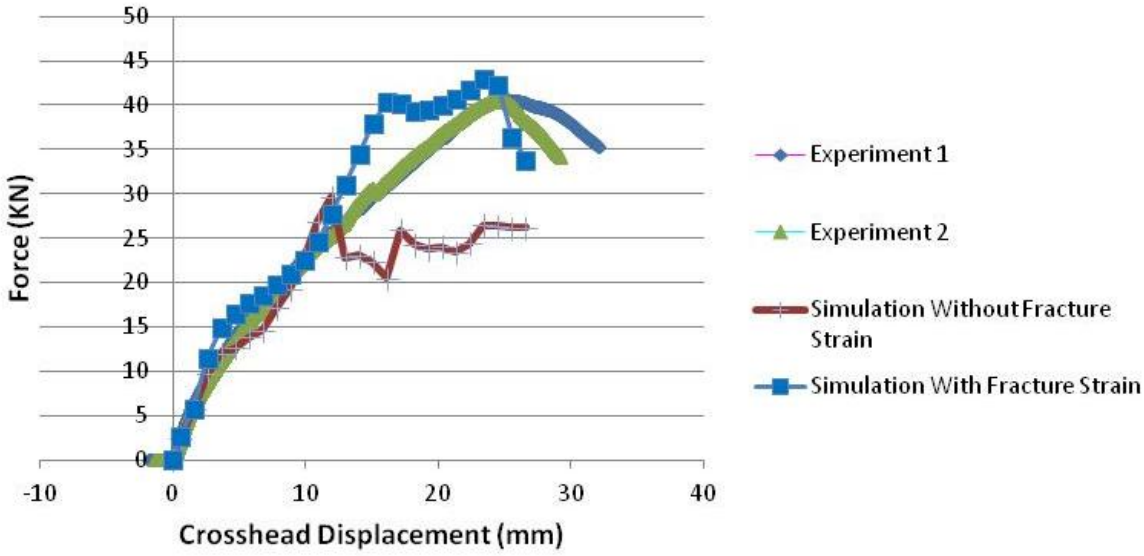

Figure 59: AM30 Four Point Bend Test Experimental and Simulation Results with and without Fracture Strain

A comparison of the results of four point bend tests for AM30 with results from [9] show that there are differences in the force path and maximum values between simulated and experimental results (Figure 60). Figure 60 shows the force path and it follows the experimental results for the most part and then it deviates at around a crosshead displacement of 15 mm. Results from [9] show that the force path goes to 0 at 2.5 mm and the force path never comes down after 25 mm. The experimental results show that the force comes down after a cross head displacement of 25 mm.

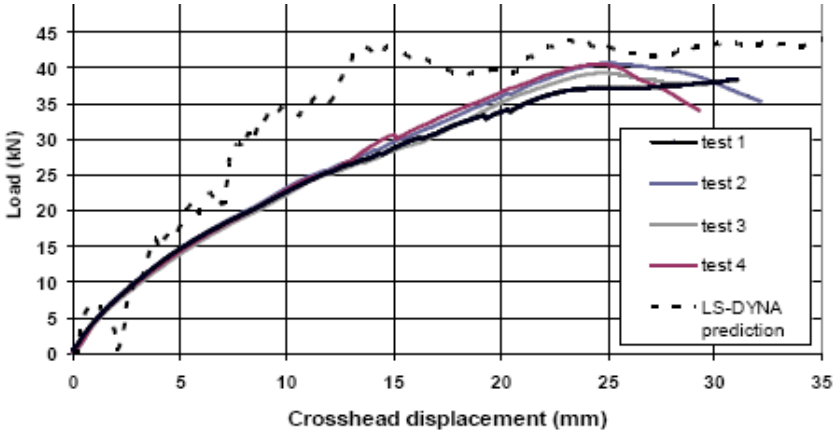

Figure 60: AM30 Four Point Bend Test Experimental and Simulated Results as Presented by Wagner et al [9]

6.3.2.3 AM60 Four Point Bend Test

The four point bending test results for AM60 are presented in Figure 61. The prediction shows that, once again, the numerical model accurately captures the trend of the experimental curves. Most of the experimental curves show a peak of 22 kN force around 18 mm displacement while the simulation results show a peak at 20 kN force at around 17 mm displacement.

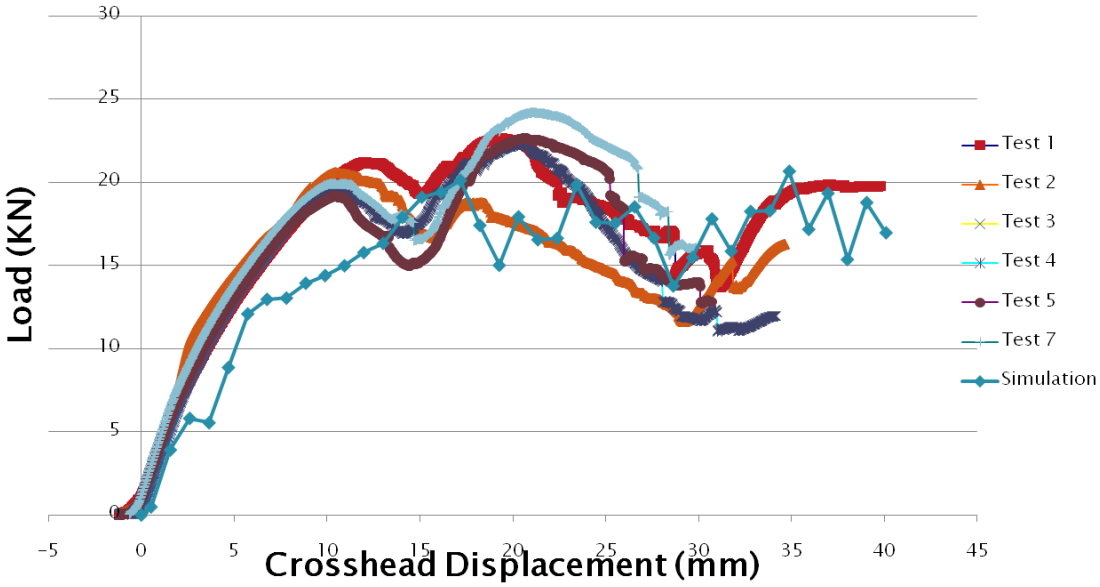

Figure 61: AM60 Four Point Bend Test Experimental and Simulated Results

There is a lot of discrepancy in the experimental curves after 27 mm but the simulated curve still predicts the overall trend with accuracy (the predicted curve lies within the experimental curves). After 27 mm displacement, it is possible that the tube was fractured and hence, all results after that point are ignored.

Comparing the results of four point bending for AM60 with results from [11] show that there are major differences between experimental and simulated results. The results from [11] deviate from the experimental force path around 5, 20 and 30 mm. The simulation is also unable to predict the peak force to acceptable accuracy. Figure 61 shows the AM60 experimental and simulated results from our failure criteria. The simulated force path remains relatively close to the experimental curves.

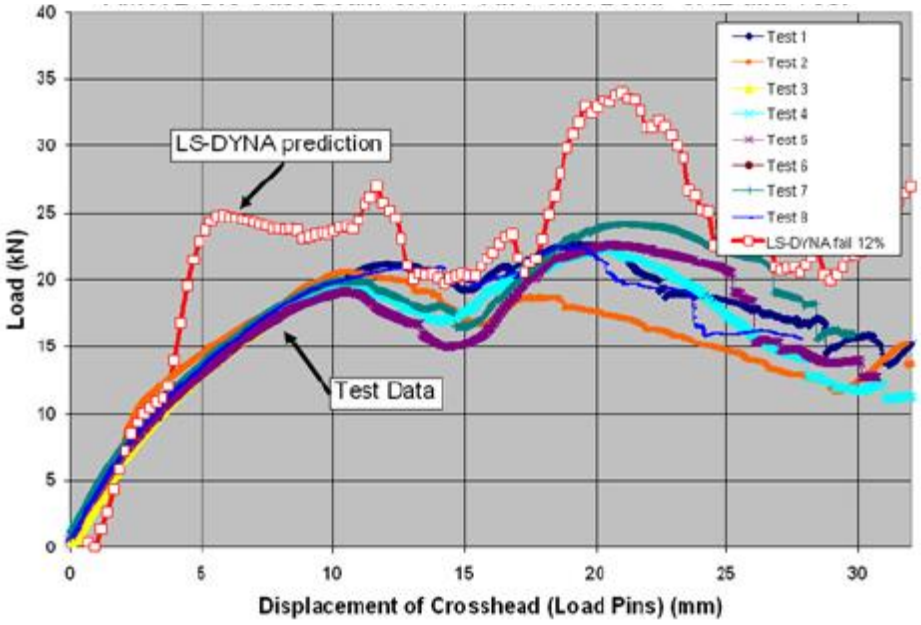

Figure 62: AM60 Four Point Bend Test Experimental and Simulated Results as Presented by Wagner et al [11]

Chapter 7
Design Modifications

In this chapter, different design concepts used to improve the performance of magnesium alloys are analyzed using the failure criterion. Four different design modifications were simulated for the three magnesium alloys (AM30, AM60 and AZ31). Some designs focus on geometrical changes while other designs use an additional material to improve the crashworthiness of magnesium tubes.

After validating the failure criterion for bending and axial crush applications, the failure criterion was used to analyze different designs. Some research with different AZ31 round tubes is presented in [59] with thin wall section tubes and aluminum-cladded magnesium tubes. This chapter provides more design modifications for AM30, AM60 and AZ31 round tubes.

It was previously mentioned that the area under the stress-strain curve provides the energy absorbed per unit volume. Stress-strain results from different simulations are compared to analyze the efficiency of different design concepts in crashworthiness applications.

7.1 Modeling

This section discusses the different designs used to test design modifications. All three magnesium alloys were simulated with different design modifications. Details about the design modifications along with any assumptions are given below.

7.1.1 Spiral Design

A spiral-shaped indentation along the surface of the tube was introduced to tubes with circular cross-sections. This design is manufactured by casting of magnesium tubes. Three different cases were analyzed with 1, 2 and 3 spirals along the surface of the tube as shown in Figure 63a-c respectively. No geometric symmetry was assumed for these simulations.

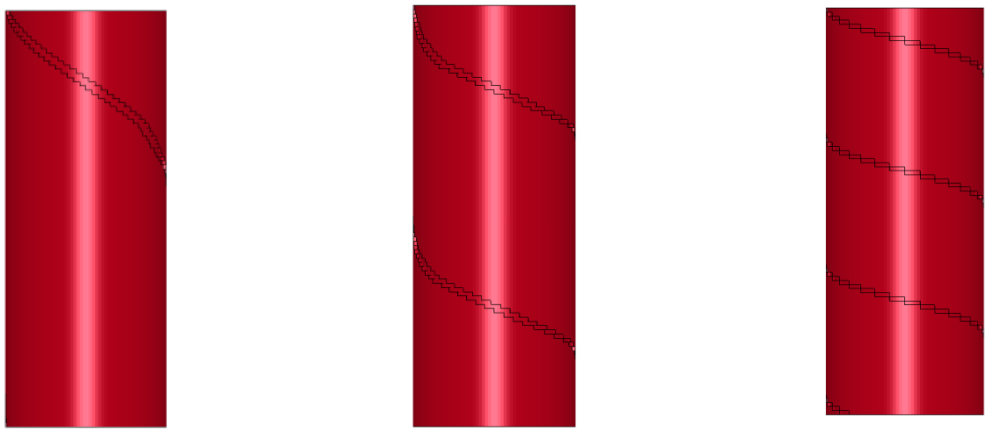

(a) (b) (c)

Figure 63: Models of Round tubes with Spirals

7.1.2 Designs with Cladding

Cladding is used to strengthen a material, reduce weight by keeping the strength the same, and to provide heat and corrosion resistance. Round magnesium tubes cladded with the aluminum alloy, 5182, were simulated for axial crush applications with varying width of aluminum and magnesium (for a constant thickness of the tube). The simulations were performed for cladding on the inside and outside of the tube. Cladding is done by welding or bonding the two tubes together [62]. It is assumed that the cladded bond is perfect.

Three different cases were analyzed with 0.5, 1.0 and 1.5 mm thickness of aluminum cladded on the inside (Figure 64a-c) and outside (Figure 65a-c) of the magnesium tubes, respectively. In these figures, red represents magnesium while blue represents aluminum (for all the models). Quarter symmetry was used for these simulations (same as Section 5.3).

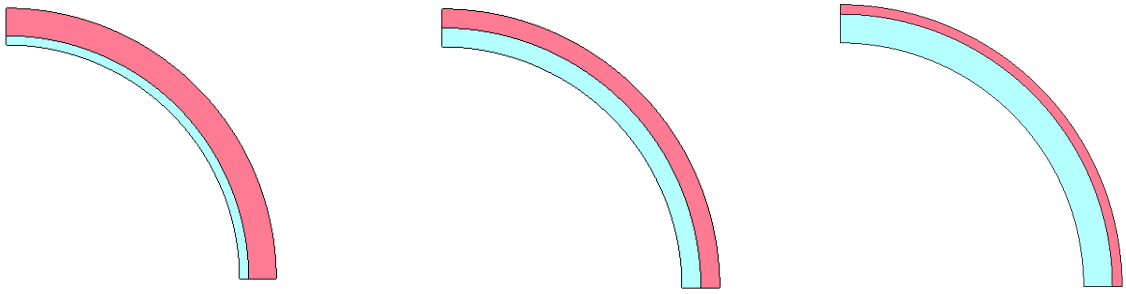

(a) (b) (c)

Figure 64: Models of Magnesium Round Tubes with Aluminum Cladding Inside the Tube with Varying Thickness

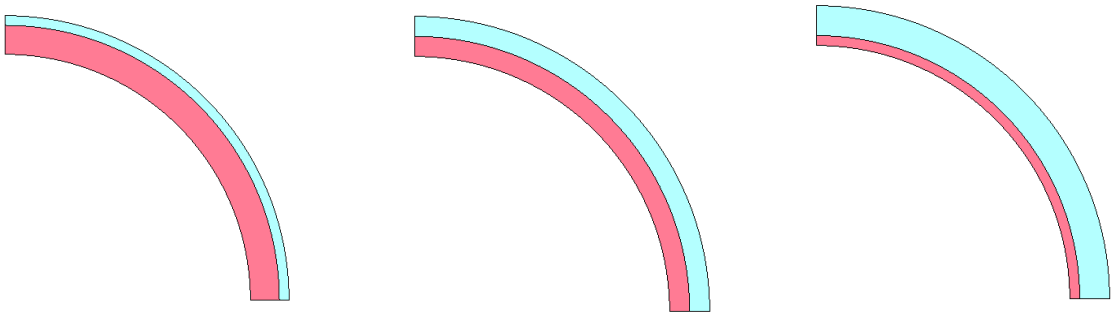

(a) (b) (c)

Figure 65: Models of Magnesium Round Tubes with Aluminum Cladding Outside the Tube with Varying Thickness

7.1.3 Longitudinal Alternating Design

Round magnesium tubes with alternating aluminum alloy, 5182, were simulated for axial crush applications with varying width of aluminum and magnesium. The aluminum and magnesium strips were joined laterally along the length of the tube. These tubes are manufactured by welding or bonding the two materials. It is assumed that the bonding between the two materials is perfect. Three different designs were analyzed with 1, 2 and 3 strips of aluminum and magnesium as shown in Figure 66a-c respectively. Once again, in these figures, red represents magnesium while blue represents aluminum. Furthermore, geometrical half symmetry was used for these simulations.

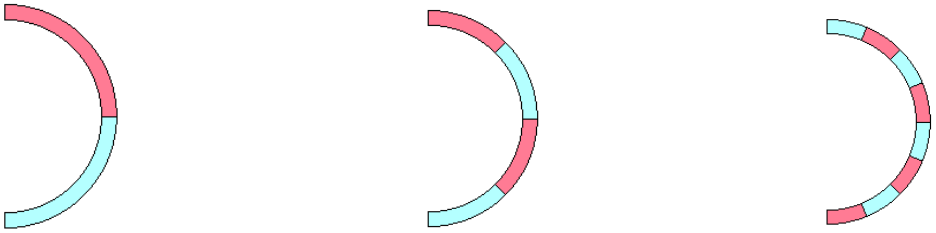

(a) **(b)** **(c)**

Figure 66: Models of Magnesium Round Tubes with Alternating Strips of Aluminum and Magnesium Laterally

7.1.4 Design with Wall Thickness Variation within the Tube

Round magnesium tubes with various wall thicknesses were simulated for axial crush applications with varying number of thinned sections indented in the tube. Thinned or cast tubes are cast and then joined by welding. Three different designs were analyzed with 1, 2 and 3 thinned sections, as shown in Figure 66a-c respectively. Geometric quarter symmetry was used for these simulations like Section 5.3.

(a) **(b)** **(c)**

Figure 67: Models of Magnesium Round Tubes with Thinned Sections

7.2 Results

This section discusses the results from the different round magnesium tube designs. All three magnesium alloys were simulated with the different design modifications. The results are compared to the round tubes with circular cross-sections for all three alloys and stress-strain curves are used to compare the simulations.

7.2.1 Spiral Design

Stress-strain response for AZ31 round tubes (up to tube failure) with spirals is shown in Figure 68. The results are compared to the round tube without spirals. Simulations show that the spiral designs absorb more energy compared to the round tube. This is mainly due to the fact that the spiral acts as a crush trigger across the length of the tube. The spiral produces buckling in the whole tube rather than just the area near the crush triggers, as it does for the round tube without spirals. Predictions show that a design with spirals can withstand up to 15% strain, while the round tube can deform up to 13% strain. The spiral designs can also handle more stress (300 MPa) before failure.

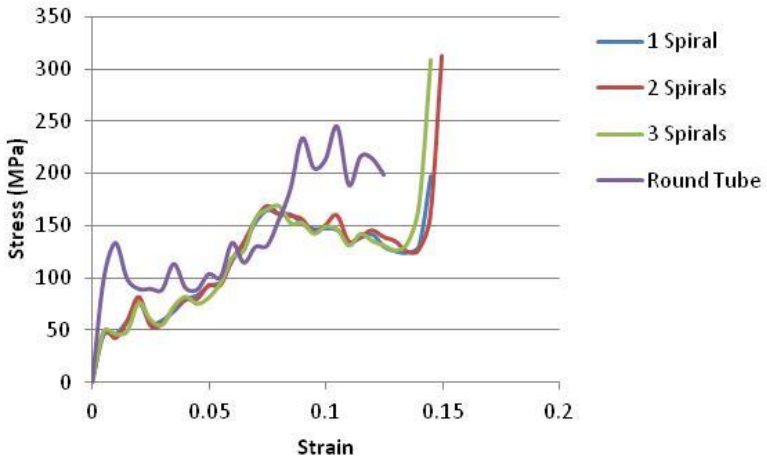

Figure 68: Simulated Stress-Strain Comparison between Different Number of Spirals on AZ31 Magnesium Round Tubes and AZ31 Round Tube

Magnesium alloy, AM30, round tube simulation results are shown in Figure 69. The results show that adding spirals in the AM30 round tube decreased the crashworthiness of the material when compared to a round tube without spirals. The round tube failed at 13% strain. The tubes with 1, 2 and 3 spirals failed at 9.5%, 10% and 11% strain respectively. Simulation results of AM60 round tubes with spirals are shown in Figure 70. The simulations show that the number of spirals on the

tube does not improve the crashworthiness of the material. The strain to failure for the round tube without spirals is around 5%. The strain to failure for the tubes with 1, 2 and 3 spirals is 3%, 3% and 4% respectively. In addition, the stress at failure for the round tube without spirals is also around 80 MPa higher than the tubes with spirals.

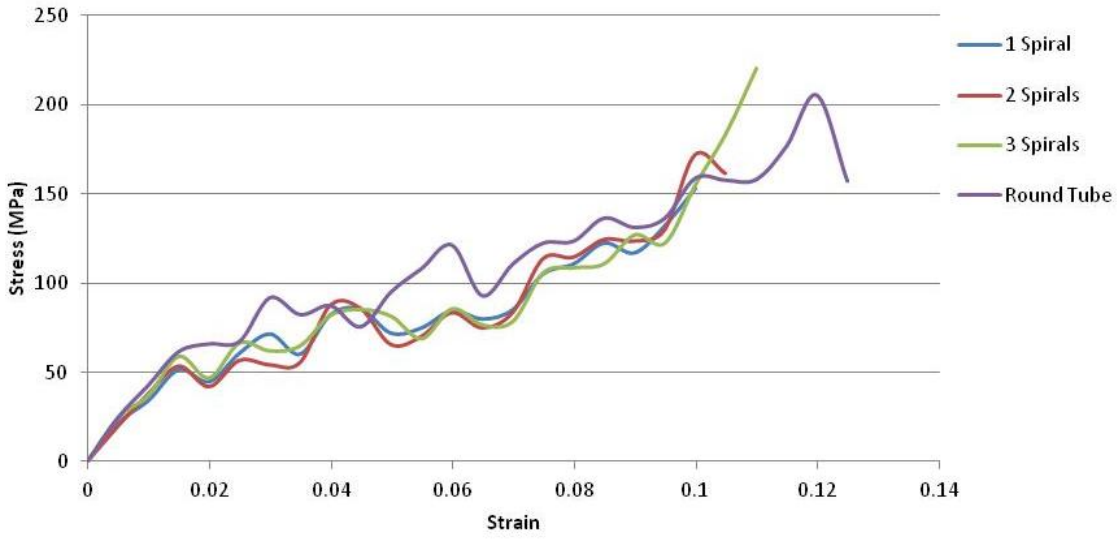

Figure 69: Simulated Stress-Strain Comparison between Different Number of Spirals on AM30 Magnesium Round Tubes and AM30 Round Tube

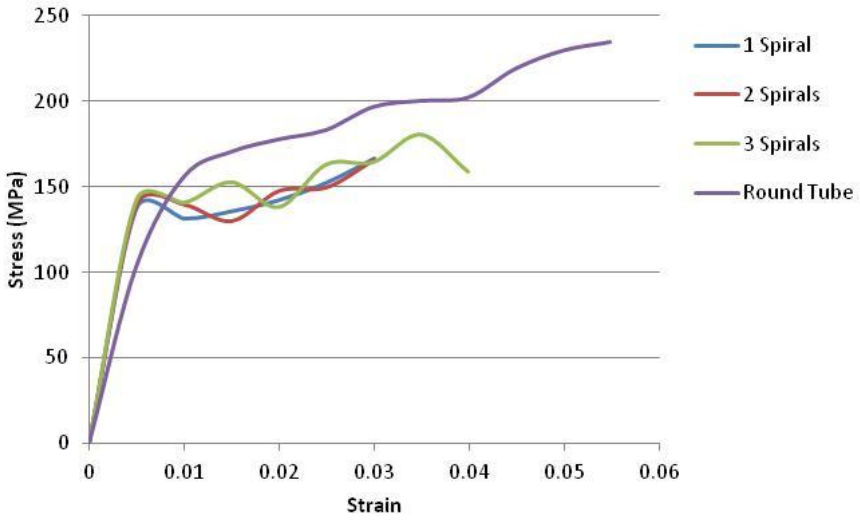

Figure 70: Simulated Stress-Strain Comparison between Different Number of Spirals on AM60 Magnesium Round Tubes and AM60 Round Tube

7.2.2 Designs with Cladding

This section provides results for AZ31, AM30 and AM60 cladded tubes. Simulations were performed with cladding on the inside and outside of the magnesium tubes. It is noted that simulation results from AZ31 cladded tubes were also presented in [57].

Stress-strain curves for AZ31 tubes cladded inside with aluminum are shown in Figure 71. The results show that the cladding improved the crashworthiness of the tube. The cladded tubes also have higher failure strain. The maximum stress is also higher for the cladded tubes. Cladded tubes with more than 0.5 mm thickness provide a failure strain of 17% while the round tube without cladding provides a failure strain of 13%. Round aluminum tube show higher failure strain but after 14% strain, the cladded tubes have a higher stress which suggests that magnesium tubes cladded with aluminum provide structural support to the tube before it fails.

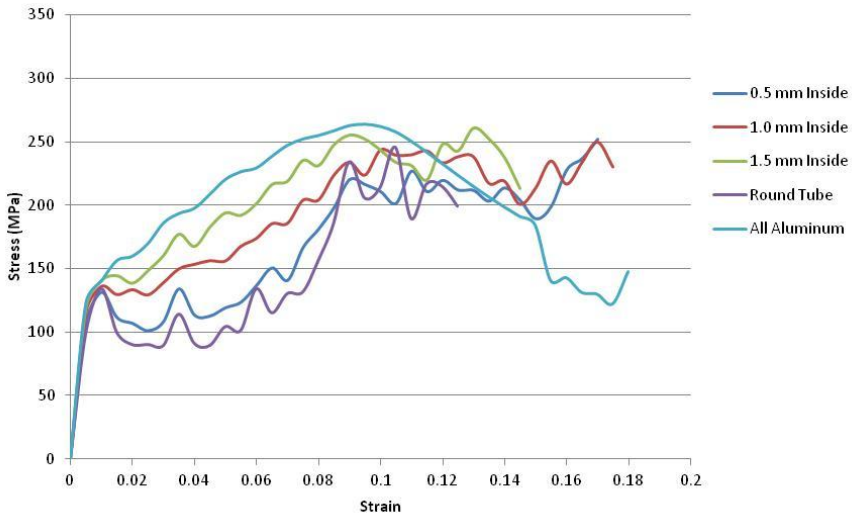

Figure 71: Simulated Stress-Strain Comparison between Different Thickness of Aluminum Cladding Inside AZ31 Magnesium Round Tubes and AZ31 Round Tube

Stress-strain curves for AM30 tubes cladded inside with aluminum are shown in Figure 72. The results show that cladding improves the crashworthiness of the tube. Furthermore, increasing the thickness of the cladding improves the crashworthiness of the tube; increasing the thickness of cladding by 0.5 mm increases the maximum stress by 50 MPa. Failure strain for all cases is roughly 11%.

Stress-strain curves for AM60 tubes cladded inside with aluminum are shown in Figure 72. The results show that the crashworthiness of the tubes increases with the thickness of cladding. However, the increase in crashworthiness for AM60 round tubes is not significant. AM60 round tube fails at around 5% strain while the AM60 cladded tubes fail at around 6%. All aluminum tubes fail after 14% strain but Figure 72 only shows the trend up to 8% strain for ease of comparison. The maximum stress for the cladded tubes is around 100 MPa higher than the round tube.

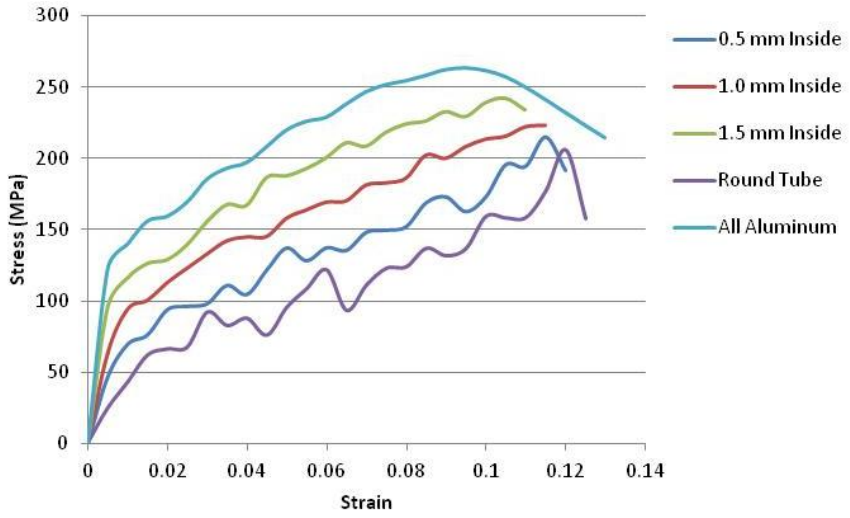

Figure 72: Simulated Stress-Strain Comparison between Different Thickness of Aluminum Cladding Inside AM30 Magnesium Round Tubes and AM30 Round Tube

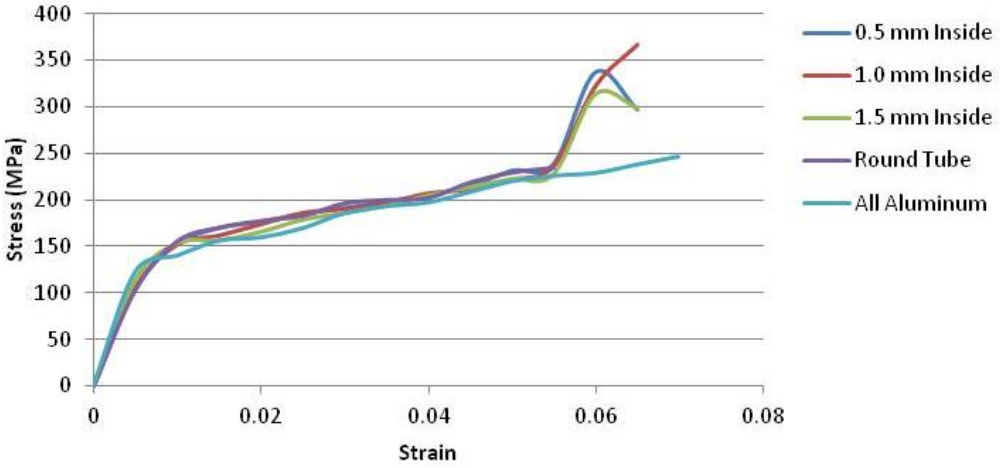

Figure 73: Simulated Stress-Strain Comparison between Different Thickness of Aluminum Cladding Inside AM60 Magnesium Round Tubes and AM60 Round Tube

Stress-strain curves for AZ31 tubes cladded outside with aluminum are shown in Figure 74. The simulations show that cladded tubes are better than the non-cladded round tubes for crashworthiness applications. Cladded tubes provide even better crashworthiness applications than all aluminum round tubes until 18% strain. Non-cladded AZ31 tubes fail at 13% strain while the cladded tubes fail at around 18% strain and at 50 MPa higher stress. The maximum stresses for the cladded tubes are also higher than those of the non-cladded round tubes.

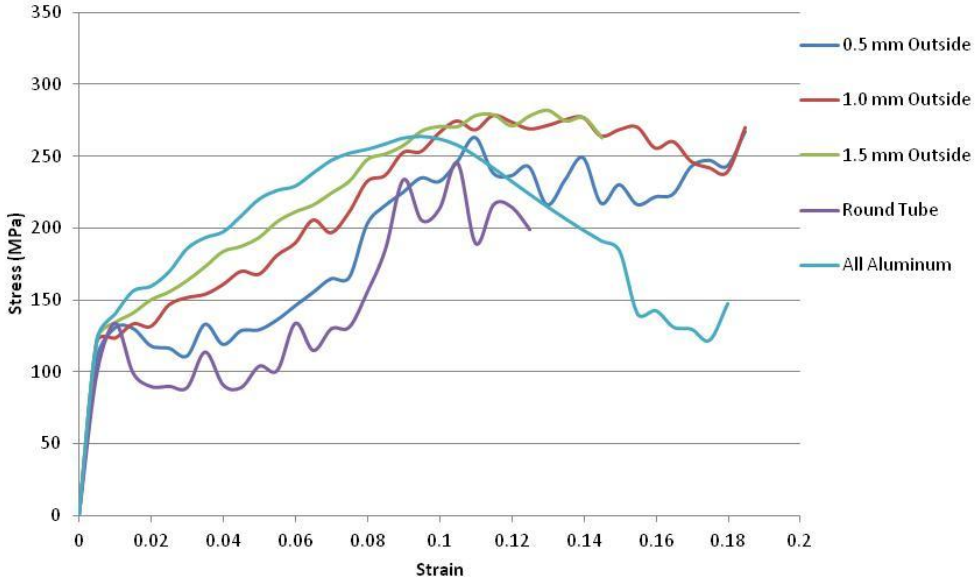

Figure 74: Simulated Stress-Strain Comparison between Different Thickness of Aluminum Cladding Outside AZ31 Magnesium Round Tubes and AZ31 Round Tube

Stress-strain curves for AM30 tubes cladded outside with aluminum are shown in Figure 75. Simulated results show better crashworthiness with increasing thickness of aluminum. The non-cladded round tube and the cladded tubes fail at around 12% strain. However, the maximum stress varies by 25 MPa as the thickness of the cladding increases.

Stress-strain curves for AM60 tubes cladded outside with aluminum are shown in Figure 76. The results show that the round tube fails at 5% strain while the cladded tubes fail at around 6% strain. Simulations show that cladding increased the crashworthiness of the tube by a small percentage.

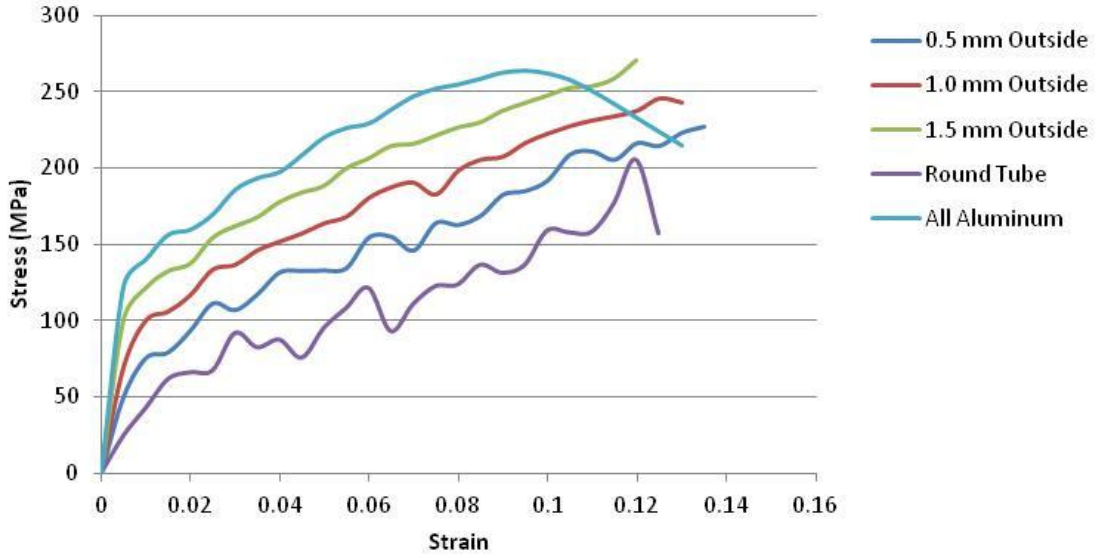

Figure 75: Simulated Stress-Strain Comparison between Different Thickness of Aluminum Cladding Outside AM30 Magnesium Round Tubes and AM30 Round Tube

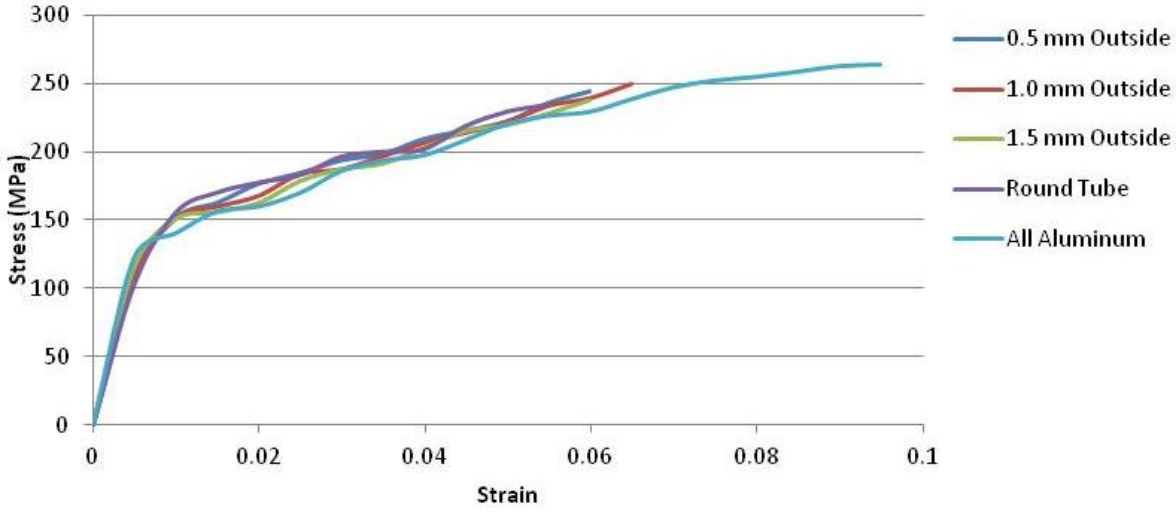

Figure 76: Simulated Stress-Strain Comparison between Different Thickness of Aluminum Cladding Outside AM60 Magnesium Round Tubes and AM60 Round Tube

7.2.3 Longitudinal Alternating Design

Stress-strain response for AZ31 round tubes with varying strips of magnesium-aluminum are shown in Figure 77. Simulations show that the magnesium-aluminum strips can absorb more energy than the round tube. Figure 77 also shows that as the number of alternating strips increases, the maximum stress increases for the same failure strain. The failure strain for all cases is around 16% while the corresponding stress is 190 MPa, 240 MPa and 270 MPa for 1, 2 and 3 strips respectively.

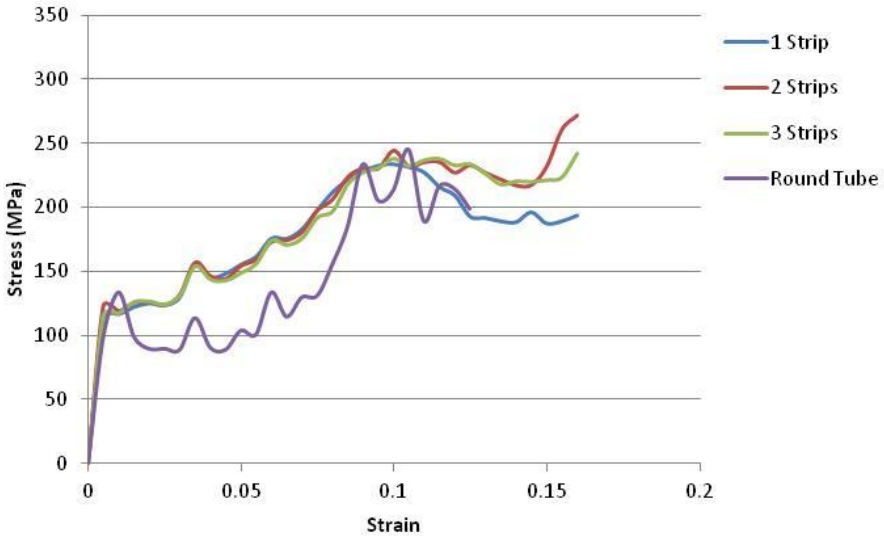

Figure 77: Simulated Stress-Strain Comparison between Round Tubes with Different Number of Alternating Strips of AZ31 and Aluminum and AZ31 Round Tube

Magnesium alloy, AM30, round tube simulation results with varying strips of magnesium-aluminum are shown in Figure 78. The simulation results show that there is a significant improvement in the crashworthiness of the material by using this method of alternating magnesium-aluminum strips. The failure strain for tubes with aluminum strips is around 11% while the round tube has a failure strain of 13%. However, the corresponding stress for the tubes with aluminum strips is 60 MPa higher than round tubes.

Simulation results of AM60 round tubes with varying strips of magnesium-aluminum are shown in Figure 79. AM60 round tubes fail at 5% strain while AM60 tubes with aluminum strips fail at 7% strain. The corresponding stress at 7% failure strain with three aluminum strips is 40 MPa higher than the round tube. It is concluded that using the aluminum strips with AM60 provides little improvement in the crashworthiness of the material.

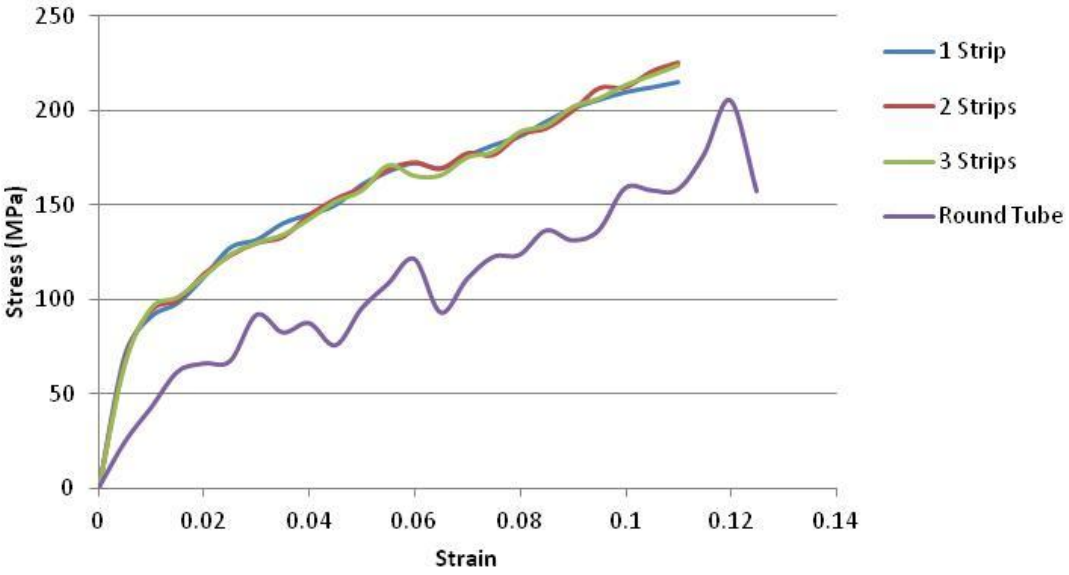

Figure 78: Simulated Stress-Strain Comparison between Round Tubes with Different Number of Alternating Strips of AM30 and Aluminum and AM30 Round Tube

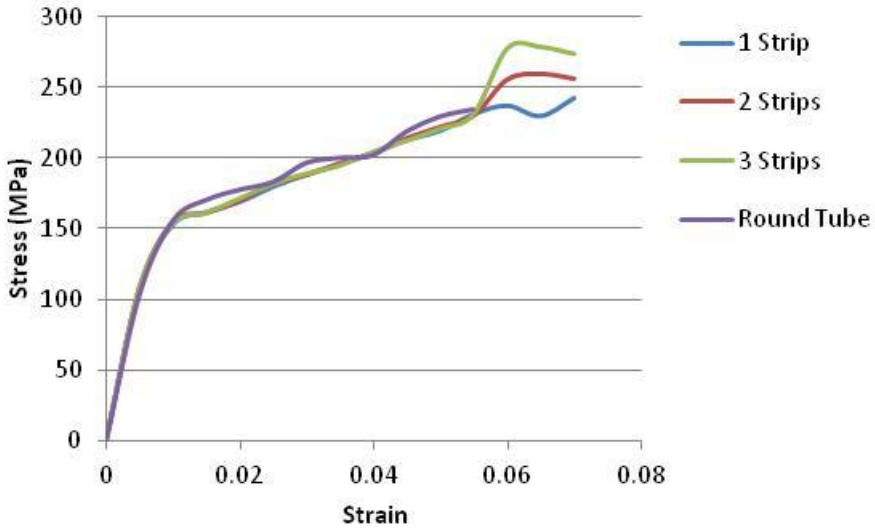

Figure 79: Simulated Stress-Strain Comparison between Round Tubes with Different Number of Alternating Strips of AM60 and Aluminum and AM60 Round Tube

7.2.4 Design with Wall Thickness Variation within the Tube

The stress-strain response for AZ31 round tubes with thinned sections is shown in Figure 80. Thinned sections were incorporated as a design modification to improve crashworthiness by providing the pre-compression needed to start buckling in the tubes. Results from Figure 80 show that the crashworthiness response for AZ31 tubes with thinned sections is less than that of the round tubes. The failure strain for tubes with and without the thinned sections is around 13%. The reason is due to the high stress concentrations in the thinned regions that lead to failure in the tube.

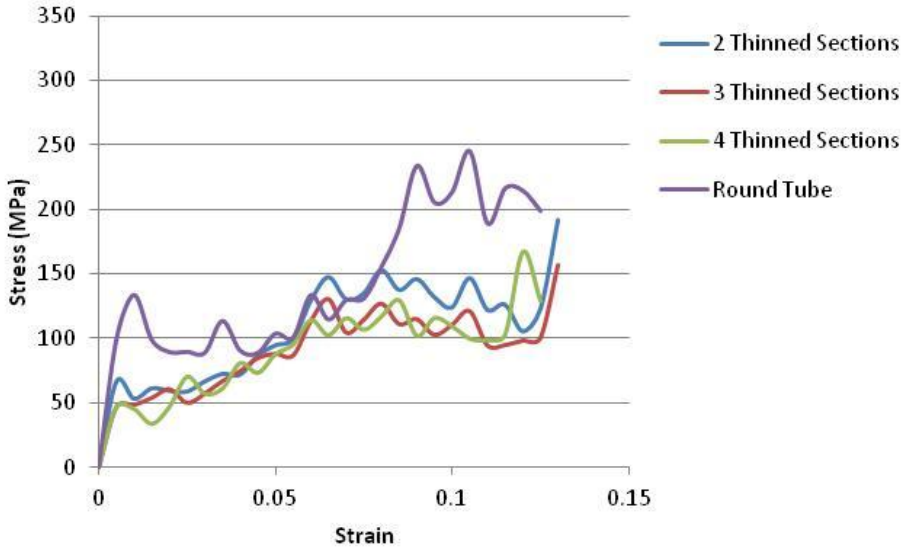

Figure 80: Simulated Stress-Strain Comparison between AZ31 Round Tubes with Different Number of Thinned Sections and AZ31 Round Tube

Magnesium alloy, AM30, round tube simulation results are shown in Figure 81. Simulation results show that the thinned regions did not improve the crashworthiness response of AM30 tubes. The failure strain for round tube is around 13% while the failure strain with the thinned sections is around 9%. The corresponding maximum stress for the thinned tubes is also lower than the round tube.

Simulations of AM60 round tubes with thinning in the wall are shown in Figure 82. Simulations show that, once again, adding thinned sections to magnesium tubes did not improve crashworthiness. In the case of AM60, the crashworthiness is less than half for tubes with thinned sections. The failure strain for AM60 round tubes and thinned tube is 5% and 3% respectively.

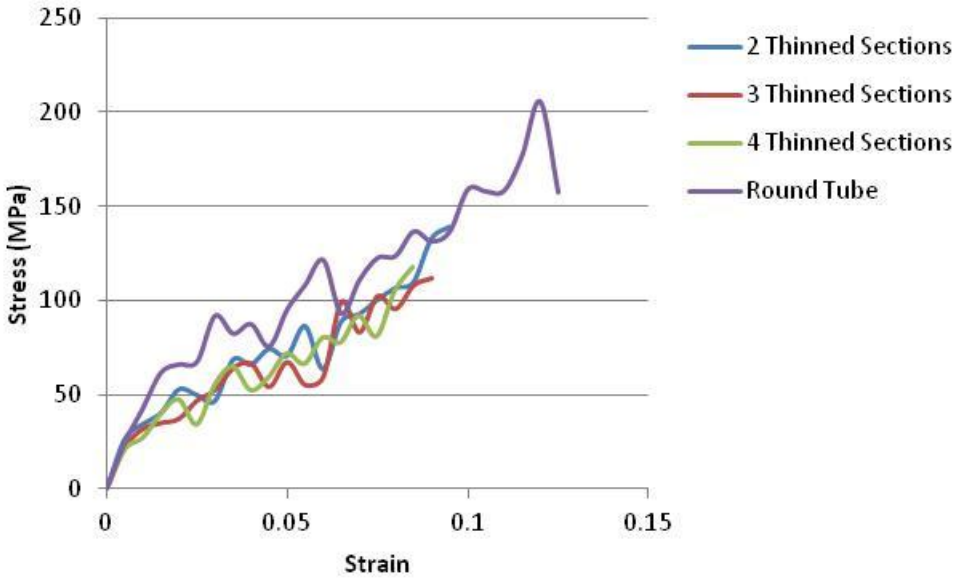

Figure 81: Simulated Stress-Strain Comparison between AM30 Round Tubes with Different Number of Thinned Sections and AM30 Round Tube

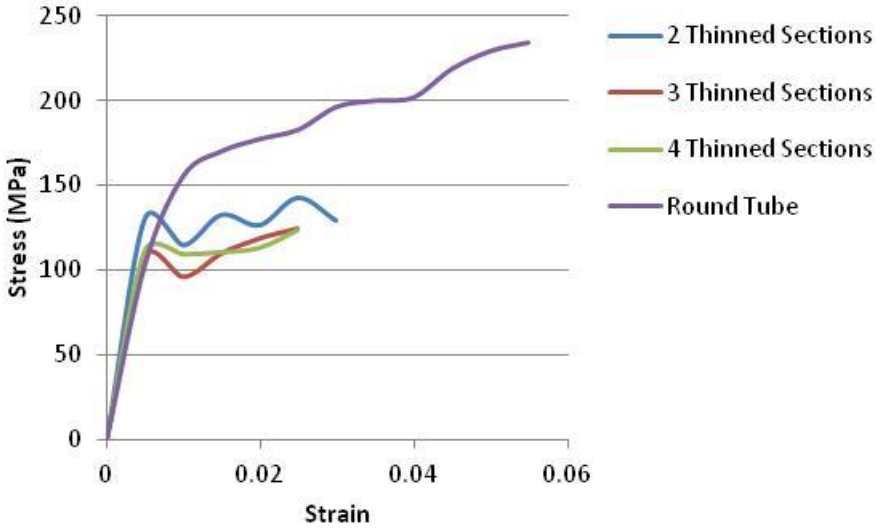

Figure 82: Simulated Stress-Strain Comparison between AM60 Round Tubes with Different Number of Thinned Sections and AM60 Round Tube

Chapter 8
Conclusions and Recommendations

8.1 Conclusions

Magnesium alloys present different challenges than other common structural metals. Magnesium alloys have asymmetric behavior under compression and tension that prevents current material models to accurately predict the behavior of magnesium alloys for crashworthiness applications. A new failure criterion that can account for the asymmetry of magnesium alloys under compression and tension was employed in this thesis for the magnesium alloys AZ31, AM30 and AM60.

The failure criterion presented in this thesis is currently the only failure criterion in literature to predict macro-scale failure in magnesium alloys. This is mainly due to the fact that the failure criterion is based on the mechanics of deformation rather than numerical exercises for curve fitting. The failure criterion was validated for bending, slow and fast axial crush. It was also applied to evaluate the performance of tubes with different designs. Furthermore, this failure criterion is a powerful tool for the automotive industry since it provides an accurate "virtual testing" environment to investigate the performance of magnesium alloys.

The criterion employed for this research took into account the maximum strain under compression and tension as well as the stresses responsible for buckling the material. The criterion also used fracture strain to find the strain at which an element fails. It is noted that the fracture strain can't be considered equal to the macroscopic failure strain if the material undergoes considerable necking. For the alloys considered in this thesis, considering the fracture strain in the neck area improved the results significantly.

The failure criterion in this thesis was used for tubes with circular cross-section. Tubes with circular cross-section are the easiest problems in terms of buckling. Thus, these simulations were only performed for AZ31 tubes and the predictions were compared to experimental observations. Furthermore, simulations were performed with different parameters and then compared to experiments.

Round tube simulations were done with imperfections to induce initial buckling. It is concluded that the imperfections placed near the top produced the best results. Quarter symmetry was used to simulate the tubes. Different load curves were also tried to produce the best results. It is concluded

that the best results were produced by instantaneous load application. This is in accordance with the experiments. Time scaling was used to reduce the time taken to perform the simulations. The most suitable time scaling factor was found by performing several simulations. Hourglass and damping was used to reduce the oscillations in the system. Oscillations in the system were assumed to be a result of the time scaling employed. Furthermore, simulations with hourglass and damping produced better results and thus, hourglass and damping were employed in the final simulations.

Simulation results for the round tube had a combination of all the simulation parameters. It is concluded that the simulations produced results with reasonable accuracy. The results matched the initial force jump with reasonable accuracy. The simulations also predicted the overall trend and the maximum force accurately.

The failure criterion was also tested on square tubes for all three alloys. Square tubes were employed in simulations of slow and fast axial crush as well as four point bending simulations. Crush simulations were done with end plugs at one end. End plugs as rigid shell elements were employed in the simulations since this approach provided the most accurate predictions. Four point tests were done with two rollers on the top and two rollers at the bottom with end plugs (at both ends). Rigid shell elements were used to simulate rollers and end plugs in the tubes. Furthermore, half symmetry was used for four point bending simulations.

AZ31 slow axial crush simulations showed geometrical similarities between the predicted and experimental deformed specimens. AM30 slow axial crush specimens predicted the bulges in the tube while the AM30 fast axial crush simulations predicted the failure points. Similarly, AM60 slow axial crush simulations predicted the failure areas accurately. It is concluded that the failure criterion predicted the geometrical features of the deformed specimens obtained from the experiments for all three magnesium alloys.

AZ31 slow and fast axial crush simulations predicted the failure point and the maximum force with reasonable accuracy when compared to experimental force-displacement curves. The simulations also predicted the overall trends of the experiments. AM30 slow axial crush simulations predicted trends but the fast axial crush simulations did not predict the trends when compared to the experiments. AM60 slow and fast axial crush simulations also predicted the trends. Furthermore, AM60 slow axial crush simulations also predicted the maximum force. The initial difference between the experimental and simulated results is possibly due to low resolution experimental sensors. It is

concluded that the failure criterion predicted the trends with good accuracy for most cases. The failure criterion also predicted the maximum force for most slow crush simulations.

Simulations of AZ31 four point bend tests were compared with experimental observations for geometrical similarities within the deformed specimens. The simulations predicted the failure point and the bulge between the top rollers. AM30 physical comparison was not available. Simulations for AM60 accurately predicted the failure points observed in the experiments. Furthermore, it is concluded that the simulations predicted the bulge between the top rollers and the failure points in all magnesium alloys.

AZ31 four point bend experiments predicted the failure point and the maximum force with good accuracy when compared to experimental force-displacement graphs. The predicted AZ31 force-displacement curve was also in good agreement with the trends of the experimental curve. AZ31 four point bend test simulations were also done using rivets. Using rigid rivets, the results showed improvements in the initial section of the force-displacement graphs. It is concluded that the combined results from simulations with and without rivets give the best results AM30 four point bending simulations initially did not predict the maximum force accurately. Due to considerable necking in AM30 samples during tensile tests, simulations were done to find the necking strain in AM30. Inputting the fracture strain into the failure criterion improved the results significantly. It is concluded that AM30 simulations with fracture strain predicted the trends and maximum force. AM60 force-displacement graphs also predicted the trend and the maximum force to general accuracy. It is concluded that the failure criterion can model the four point bend tests reasonably accurately for all three alloys.

Simulation results from AZ31 round tubes were used to analyze different design modifications. Stress-strain results from these modifications were compared with plain round tubes for analyzing their use in crashworthiness applications.

Magnesium round tubes were compared to round magnesium tubes with spiral design indented on them. AZ31 spiral tubes showed higher peak stress than the plain round tube and an increase in crashworthiness. AM30 and AM60 tubes showed lower failure strain than the round tube. It is concluded that the spiral design increased the crashworthiness of AZ31 tubes only.

Magnesium tubes cladded with various thicknesses of aluminum were also compared to round tubes. When aluminum was cladded inside the magnesium tube, AZ31 tubes showed improved

crashworthiness at higher failure strain and maximum stress. AM30 tubes also showed improved crashworthiness than the round tube. However the failure strain for cladded AM30 tubes was very close to the failure of the round tube. AM60 cladded tubes show a higher maximum stress than the round tubes but there wasn't a significant increase in the failure strain and crashworthiness of the material. It is concluded that AZ31 and AM30 cladded tubes show an improvement in crashworthiness. AM60 cladded tubes did not show a considerable improvement when cladded. It is concluded that the improvement in crashworthiness for AM60 tubes is possibly offset by the cost of the process.

Magnesium tubes cladded with aluminum on the outside surface were also simulated. AZ31 tubes showed a higher failure strain than round tubes. The corresponding stress for cladded AZ31 tubes was higher than the plain round tube and an all-aluminum round tube. AM30 cladded tubes show an improvement in crashworthiness than the plain round tube with the same failure strain. AM60 tubes did not show a considerable increase in crashworthiness. It is concluded that the AZ31 and AM30 cladded tubes showed an improvement in crashworthiness of the materials with increased thickness of cladding. It is also concluded that AM60 cladded tubes showed little improvement over the round tube.

Magnesium tubes were also compared to plain round tubes with alternating magnesium-aluminum strips. AZ31 magnesium-aluminum tubes had higher crashworthiness than the plain round tube due to higher failure strain. However, the maximum stress was same for both cases. AM30 magnesium-aluminum tubes show very high improvement in crashworthiness when compared to plain round tubes due to high peak stress. AM60 tubes showed little improvement in crashworthiness but the crashworthiness improved with increasing number of alternating strips. It is concluded that both AM30 and AZ61 showed improvement in crashworthiness with the introduction of magnesium-aluminum strips. AM60 showed little improvement with higher maximum stress than the round tube.

Magnesium tubes were also simulated with thinned sections in the tube. AM30, AM60 and AZ61 simulations did not show any improvement in crashworthiness of the tube. It is concluded that the thinned sections used to induce buckling resulted in areas with high stress that led to an early failure of the tube.

8.2 Recommendations

Crashworthiness of magnesium alloys is a relatively new field. Its application in the automotive industry is still under research. The proposed failure criterion provides an important understanding to predict failure in magnesium alloys under compressive loading. Some recommendations to further improve the failure criterion are:

a. Explore the possibility of using stress triaxiality to fail an element as suggested by Johnson Cook Fracture Model [40].

b. Explore the maximum shear criteria for magnesium alloys [39]. The current model does not consider shear failure in the model.

c. Perform crashworthiness tests at different strain rates and implement the effect of strain rates on crashworthiness of magnesium alloys.

References

[1] J Rossiter, K Inal, and R K Mishra, "Numerical Modeling of Failure in Magnesium Alloys during Crush Simulations," in *Magnesium Technology*, 2010.

[2] D G Tari and M J Worswick, "Experimental Investigation of anisotropy evolution of AZ31 magnesium alloy sheets under tensile loading," in *ESAFORM*, 2011, pp. 1547-1552.

[3] X Chen and et al, "Study of Die Cast Magnesium Components for Crash Safety," *IJ Crash*, pp. 429-440, 2002.

[4] S Logan and et al, "Lightweight Magnesium Intensive Body Structure," in *SAE Technical Paper*, 2006.

[5] D. Eliezer, E. Aghion F.H. Froes, "The Science, Technology, and Applications of Magnesium," *JOM Journal of the Minerals, Metals and Materials Society*, vol. 50, no. 9, pp. 30-34, Sep. 1998.

[6] A.K. Sachdev A.A. Luo, "Magnesium Wrought Alloy Having Improved Extrudability and Formability," US Patent Application, March 4, 2004.

[7] A A Luo, "Wrought Magnesium Alloys and Manufacturing Processes for Automotive Applications," in *SAE Technical Paper*, 2005, pp. 2005-01-0734.

[8] American Metal Market, "Metal Statistics," May 2004.

[9] D Wagner and et al, "Test Results and FEA Predictions from Magnesium AM30 Extruded Beams in Bending and Axial Compression," in *Magnesium Technology*, 2009, pp. 541-549.

[10] J H Song, H Wang, and T Belytschko, "A comparative study on finite element methods for dynamic fracture," *Comput Mech*, vol. 42, pp. 239-250, 2008.

[11] D A Wagner, S D Logan, K Wang, and et al, "FEA Predictions from Magnesium Beams in Bending and Axial Compression," in *SAE Technical Paper*, 2010.

[12] D Wagner and et al, "Test Results and FEA Predictions from Magnesium AZ31 Sheet Beams in Bending and Axial Compression," in *Magnesium Technology*, 2010.

[13] A. Beck,. London: F.A. Hughes & Co. Ltd, 1941, p. 374.

[14] I.J. Polmear,., 1994, ch. 10, pp. 1-14.

[15] C J. Bettles and M A. Gibson, "Current Wrought Magnesium Alloys: Strengths and Weaknesses," *JOM Journal of the Minerals, Metals and Materials Society*, vol. 57, pp. 46-49, 2005.

[16] Su-Hyeon Kim, Bong-Sun You, Chang Dong Yim, and Young-Myoung Seo, "Texture and microstructure changes in asymmetrically hot rolled AZ31 magnesium alloy sheets," *Materials Letters*, vol. 59, pp. 3876-3880, April 2005.

[17] Lan Jiang, John J. Jonas, Alan A. Luo, Anil K. Sachdev, and Ste´phane Godet, "Twinning-induced softening in polycrystalline AM30 Mg alloy at moderate temperatures," *Scripta Materilia*, vol. 54, pp. 771-775, December 2006.

[18] K. Máthis, F. Chmelık, Z. Trojanová, P. Lukác, and J. Lendvai, "Investigation of some magnesium alloys by use of the acoustic emission technique," *Materials Science and Engineering*, pp. 331-335, December 2004.

[19] R. Hill, "A Theory of the Yielding and Plastic Flow of Anisotropic Metals," *Proceedings of the Royal Society of London. Series A, Mathematical and Physical Sciences*, vol. 193, no. 1033, pp. 281-297, March 1948.

[20] J. S. Kallend and U. F. Rollet, "Operational texture analysis.," *Material Science & Engineering*, vol. 132, pp. 1-11, 1991.

[21] J. A. Del Valle and O. A. Ruano, "Effect of annealing treatments on the anisotropy of magnesium alloy sheet processes by severe rolling."," *Materials Letters*, vol. 63, pp. 1551-1554, 2009.

[22] O. Cazacu, B. Plunkett, and F. Barlat, "Orthotropic yield criterion for hexagonal closed packed metals," *International Journal of Plasticity* , vol. 22, pp. 1171-1194, 2006.

[23] B.L. Tiwari, A.K. Sachdev, and J.L. Bommarito, "Magnesium Extrusions: Alloy and Process Development," GM R&D unpublished research.,.

[24] "Timminco Magnesium Wrought Products," Timminco Corporation Brochure, Aurora, CO, 1998.

[25] A.A. Luo and A.K. Sachdev, "Development of A Moderate Temperature Bending Process For Magnesium Alloy Extrusions," in *International Conference on Magnesium*, Beijing, China, 2004.

[26] P.E. Krajewski, "Elevated Temperature Forming of Sheet Magnesium Alloys," in *Magnesium Technology 2002*, Warrendale, PA, 2002, pp. 175-179.

[27] T Wierzbicki, Y Bao, and et al, "Calibration and evaluation of seven fracture models," *International Journal of Mechanical Sciences*, vol. 47, pp. 719-743, 2005.

[28] T Wierzbicki and L. Xue, "On the effect of the third invariant of the stress deviator on ductile fracture. Impact and Crashworthiness Lab Report #136," *International Journal of Fracture*, 2005, Submitted for publication.

[29] M. G. Cockcroft and D. J. Latham, "Ductility and the workability of metals," *Journal Institute of Metals*, vol. 96, pp. 33-39, 1968.

[30] P. Brozzo, B. Deluca, and R. Rendina, "A new method for prediction of formability limits in metal sheets," in *Sheet Metal Forming and Formability: Proceedings of the 7th biennial conference of the International Deep Drawing Research group*, 1972.

[31] A. K. Ghosh, "A criterion for ductile fracture in sheets under biaxial loading," *Metallurgical and Materials Transactions*, vol. 7A, pp. 523-533, 1976.

[32] D. M. Norris, J. E. Reaugh, B. Moran, and D. F. Quinnones, "A plastic strain mean-stress criterion for ductile fracture," *Journal of Engineering Materials Technology*, vol. 100, pp. 279-286, 1978.

[33] M. Oyane, T. Sato, K. Okimoto, and S. Shima, "Criteria for ductile fracture and their applications," *Journal of Mechanical Working Technology*, vol. 4, pp. 65-81, 1980.

[34] A. G. Atkins, "Possible explanation for unexpected departures in hydrostatic tension-fracture strain relations," *Metal Science*, vol. 15, pp. 81-83, 1981.

[35] M. L. Wilkins, R. D. Streit, and J. E. Reaugh, "Cumulative-strain-damage model of ductile fracture: simulation and prediction of engineering fracture tests," Lawrence Livermore National Laboratory, Technical report UCRL-53058 1980.

[36] GR Johnson and WH Cook, "Fracture characteristics of three metals subjected to various strains, strain rates, temperatures and pressures," *Engineering Fracture Mechanics*, vol. 21, pp. 31-48, 1985.

[37] Kuroda M and Tvergaard V, "Forming limit diagrams for anisotropic metal sheets with different yield criteria," *International Journal of Solids and Structures*, vol. 31, pp. 5037-5059, 2000.

[38] NT Huber, "Contribution to the foundation of the strength of the material," *Czasopismo Techniczne*, pp. 22-81, 1904.

[39] JP Bardet, "Lode dependences for isotropic pressure-sensitive elastoplastic materials," *Transactions of the ASME*, vol. 57, pp. 498-506, 1990.

[40] D Bigoni and A Piccolroza, "A new yield function for geomaterials," , Napoli, 2003, p. 226.

[41] M Aghaie-Khafri, R Mahmudi, and H Pishbin, "Role of yield criteria and hardening laws in the prediction of forming limit diagrams," *Metallurgical and Materials Transactions A*, vol. 33A, pp. 1363-1371, 2002.

[42] Z Marciniak and K. Kuczynski, "Limit strain in the processes of stretch-forming sheet metal," *International Journal of Mechanical Sciences*, vol. 9, pp. 609-620, 1967.

[43] B Bourdin, GA Francfort, and JJ Marigo, "Numerical experiments in revisited brittle fracture," *J Mech Phys Solids*, vol. 48, no. 4, pp. 797-826, 2000.

[44] Domenico Umbrello, "Finite element simulation of conventional and high speed machining of Ti6Al4V alloy," *Journal of Materials Processing Technology*, vol. 196, pp. 79-87, May 2007.

[45] H.C. Lee, J.S. Choi, K.H. Jung, and Y.T. Im, "Application of element deletion method for numerical analyses of cracking ," *Journal of Achievements in Materials and Manufacturing Engineering*, vol. 25, no. 2, pp. 154-161, August 2009.

[46] T Belytschko, H Chen, J Xu, and G Zi, "Dynamic crack propagation based on loss of hyperbolicity with a new discontinuous enrichment," *Int J Numer Meth Eng*, vol. 58, pp. 1873–1905, 2003.

[47] J-H Song, PMA Areias, and T Belytschko, "A method for dynamic crack and shear band propagation with phantom nodes," *Int J Numer Meth Eng*, vol. 67, pp. 868–893, 2006.

[48] M Ortiz and ` A Pandolfi, "A class of cohesive elements for the simulation of three-dimensional crack propagation," *Int J Numer*, vol. 44, pp. 1267-1282, 1999.

[49] X-P Xu and A Needleman, "Numerical simulation of fast crack growth in brittle solids," *J Mech Phys Solids*, vol. 42, no. 9, pp. 1397–1434, 1994.

[50] G Camacho and M Ortiz, "Computational modeling of impact damage in brittle materials," *Int J Solid Struct*, vol. 33, pp. 2899-2938, 1996.

[51] T Belytschko, Lu Y, and Gu L, "Element free Galerkin methods," *International Journal for Numerical Methods in Engineering*, vol. 37, pp. 229-256, 1994.

[52] JM Melenk and I. Babuska, "The partition of unity finite element method: Basic theory and applications," *Computer Methods in Applied Mechanics and Engineering*, vol. 39, pp. 289-314, 1996.

[53] T Belytschko, T Krongauz, and et al, "Meshless Methods: An Overview and Recent Developments," *Computer Methods in Applied Mechanics and Engineering*, vol. 139, pp. 3-47, May 1996.

[54] Livermore Software Technology Corporation, "LS-DYNA Keyword User Manual ," Livermore Software Technology Corporation, 2006.

[55] W Muhammad, "Axial Crush of Round Magnesium Tube Using Incremental Plasticity," University of Waterloo, 2011.

[56] Livermore Software Technology Corporation, "LS-DYNA Theory Manual, Version 970," Livermore Software Technology Corporation, 2003.

[57] Jonathan Rossiter, Kaan Inal, and Raj Mishra, "Numerical modeling of the failure of magnesium tubes under compressive loading," *Journal of Engineering Science and Technology*, 2011, Accepted.

[58] J Kang et al., "Constitutive behavior of AA5754 Sheet Materials at Large Strains," *Journal of Engineering Materials and Technology*, vol. 130, 2008.

[59] Jonathan Rossiter and et al, "Numerical Modeling of Failure in Magnesium Alloys during Crush Simulations," in *Magnesium Technology 2010*, 2010.

[60] Dan Hasenpouth, "Tensile High Strain Rate Behavior of AZ31B Magnesium Alloy Sheet," University of Waterloo, Masters Thesis 2010.

[61] X Huang, G Lu, and et al, "Energy absorption in splitting square metal tubes," *Thin-Walled Structures*, vol. 40, no. 2, pp. 153-165, 2002.

[62] JFE. (2011, December) CLAD STEEL PLATE. [Online]. http://www.jfe-steel.co.jp/en/products/plate/catalog/c1e-009.pdf

[63] A A luo, "Wrought Magnesium Alloys and Manufacturing Processes for Automotive Applications," in *SAE Technical Paper*, 2005, pp. 2005-01-0734.

[64] Sabrina Alam Khan, Yukio Miyashita, Yoshiharu Mutohc, and Toshikatsu Koike, "Fatigue behavior of anodized AM60 magnesium alloy under humid environment," *Materials Science and Engineering A*, vol. 498, pp. 377-383, 2008.